A decoupled SPH-FEM analysis of hydrodynamic wave pressure on hyperbolic-paraboloid thin-shell coastal armor and corresponding structural response

Article *in* Engineering Structures · October 2022

DOI: 10.1016/j.engstruct.2022.114738

3 authors, including:

Gaoyuan Wu
Princeton University
5 PUBLICATIONS **4** CITATIONS
SEE PROFILE

Shengzhe Wang
University of Colorado
31 PUBLICATIONS **210** CITATIONS
SEE PROFILE

A Decoupled SPH-FEM Analysis of Hydrodynamic Wave Pressure on Hyperbolic-Paraboloid Thin-shell Coastal Armor and Corresponding Structural Response

Gaoyuan Wu*, Maria Garlock, Shengzhe Wang

Department of Civil and Environmental Engineering, Princeton University, Princeton, NJ 08544, United States

*Corresponding author.

Email addresses: gaoyuanw@princeton.edu (G. Wu), mgarlock@princeton.edu (M. Garlock), shengzhe@princeton.edu (S. Wang).

This Preprint was accepted by Engineering Structures and the published journal article is available online.

DOI: https://doi.org/10.1016/j.engstruct.2022.114738

ABSTRACT

Kinetic Umbrella, an innovative thin-shell structural system, incorporating hyperbolic paraboloid (hypar) geometry, has been proposed for coastal hazard mitigation. Its feasibility against surge and wave loadings has been conceptually validated via a Hurricane Sandy case study. However, the typical hydrodynamic wave pressure on hypar geometries and the rationality of the previously conducted static structural analyses remain unknown. In response, this paper implements a decoupled numerical scheme consisting of smoothed particle hydrodynamics (SPH) and finite element modeling (FEM), investigating the hydrodynamic wave pressure and corresponding structural response via structural dynamic analyses. Furthermore, the accuracy of applying the hydrodynamic wave pressure predicted by the well accepted Goda's formula to the structural analysis of Kinetic Umbrellas is also evaluated. The results show that the hydrodynamic wave pressure on hypar follows a bilinear like shape along height and increases gradually from the edge of the hypar to the longitudinal spine. The hydrodynamic wave pressure difference between the edge and the longitudinal spine will be intensified by higher warping magnitude of hypar and under breaking waves. For structural response, the maximum displacement and the maximum tensile membrane force of the shell are significantly underestimated by static analyses with Goda's formula, implying the necessity of implementing the decoupled SPH-FEM scheme with structural dynamic analyses. For other critical demands, the difference is mostly smaller than 20%. The findings reinforce the idea that hypar thin shells are structurally feasible under surge and wave loadings, and ultimately facilitate the employment of hypar thin shells for coastal defense as a sustainable alternative to traditional coastal structures.

Keywords: smoothed particle hydrodynamics (SPH), finite element modeling (FEM), hyperbolic paraboloid (hypar), wave structure interaction (WSI), Goda wave pressure formulae, thin shell, Kinetic Umbrellas

1 INTRODUCTION

Over the last few decades, concerns about how climate change is going to impact structural design have emerged [1]. The potential consequences of climate change include sea-level rise and storm surge combined with strong waves, which are all closely related to the design of structures offshore and near the shoreline [2–4]. Gravity-based seawalls and breakwaters are the major types of structures that shield the nearshore community, but there exist unwanted environmental, economic, and social impacts brought by these structures beside their ability to protect the community [5–7]. Thus, one underlying challenge in structural engineering in the context of climate change is to sustainably design structures for coastal defense that minimize the unwanted environmental, economic, and social impacts.

The authors have been researching thin-shell Kinetic Umbrella, a structural system for coastal hazard mitigation incorporating hyperbolic paraboloid (hypar) geometry [8]. Kinetic Umbrellas stay in the upright position when operating normally (Fig. 1.b), providing shade and resting area for the community, and transform to coastal armor (Fig. 1.c) when needed, protecting the coastline. Compared to traditional structures (Fig. 1.a), the Kinetic Umbrella is elegant in shape, protects the community without blocking the access to the beach and the views, and consumes less material. Studies have been done to show the feasibility under inundation and the capability to suppress wave overtopping induced by landfalling hurricanes [9,10]. The transformation kinematics design, and a case study of the feasibility against Hurricane Sandy have further validated the applicability [11,12]. Even without the kinetic feature, the thin-shell hypar is a good candidate for future coastal defense, replacing the gravity-based structures that consume a lot of material, and being in

Fig. 1. a) Seawall at Monmouth Beach, NJ; b) Upright Kinetic Umbrellas; c) Tilted Kinetic Umbrellas for coastal defense

accordance with sustainability as the cement industry is responsible for 7% of CO_2 generated on earth [13]. However, there are a few questions yet to be addressed. First, the typical wave pressure distribution on hypar geometry is still unknown, which poses questions on understanding the mechanism of how hypar geometry resists wave loading. Second, whether the widely used Goda’s formula [14–16] is applicable for estimating the wave pressure on hypar geometry is another significant question. Furthermore, the static structural analysis implemented in previous studies may underestimate the critical demands as the wave loading is essentially hydrodynamic. As a result, studies exploring the pressure distribution on hypar geometry are needed and structural dynamic analysis should be conducted to further prove the validity of such thin-shell structures.

Smoothed Particle Hydrodynamics (SPH) is a numerical method for solving computational fluid dynamics (CFD) problems and has gained a growing popularity recently with the improvement of hardware capacity and parallel computing programming [17]. One of most significant advantages of SPH over other CFD methods is that SPH is a mesh-free method [18], which enables efficient transformations of complex fluid domains and structures to discrete particles [19]. DualSPHysics [17], an open-source SPH solver that utilizes parallel computing of graphical processing units (GPUs) to improve the computational efficiency [20], is widely used. Studies have shown the accuracy of DualSPHysics: Altomare et al. [21] reproduced the wave force on structures and showed that the solver could generate accurate results by comparing SPH models to empirical formula and physical experiments; Barreiro et al. [22] validated the solver through dam-break experiments; Zhang et al. [23] simulated the interaction between ocean waves and breakwaters, and validated the results using physical experiments; Dang et al. [24] implemented the solver and compared the wave forces for various coastal structures. However, the studies above mainly focus on the wave pressure at only few points or the total reaction force of the structures, which does not include detailed pressure distribution study on the structures and further structural analysis. Wang et al. proposed [8] a decoupled scheme incorporating SPH and finite element modeling (FEM) that enables a full analysis of wave-structure interaction (WSI), but the force calculation method is not robust and may require an extremely fine resolution to obtain accurate results. As a result, a modification of such decoupled SPH-FEM scheme is proposed herein to tackle the interested problems.

This objective of this paper is to fill in these knowledge gaps identified by the literature review: (1) presenting a more robust SPH-FEM mapping method for the simulations of wave-shell interaction, (2) understanding the typical hydrodynamic wave pressure distribution on hypar geometries, (3) studying the structural response of Kinetic Umbrellas against waves via structural dynamic analysis, and (4) evaluating the applicability of Goda’s formula to hypar shaped

Kinetic Umbrellas. This paper is organized as follows. Section 2 introduces this widely used Goda's formula and different types of wave loadings. Section 3 introduces the proposed decoupled SPH-FEM technique. Section 4 presents a parametric study to understand the typical wave pressure distribution on hypar and corresponding structural response, where a validation of the SPH scheme is illustrated at the beginning. The conclusions are summarized in Section 5.

2 Wave Pressure on Structures

Coastal structures are subjected to hydrostatic loading from inundation and hydrodynamic loading from waves (Fig. 2). For seawall-type structures, the maximum total loading during a wave strike is the summation of hydrostatic loading and the maximum hydrodynamic wave loading (Fig. 2) whereas for breakwater-type structures, the maximum total loading only comes from the waves since the hydrostatic component is balanced by the water on the front and back side. For this study, Kinetic Umbrellas work like seawalls and thus, the total loading includes both the hydrostatic part and hydrodynamic part.

2.1 Wave Pressure Formula by Goda

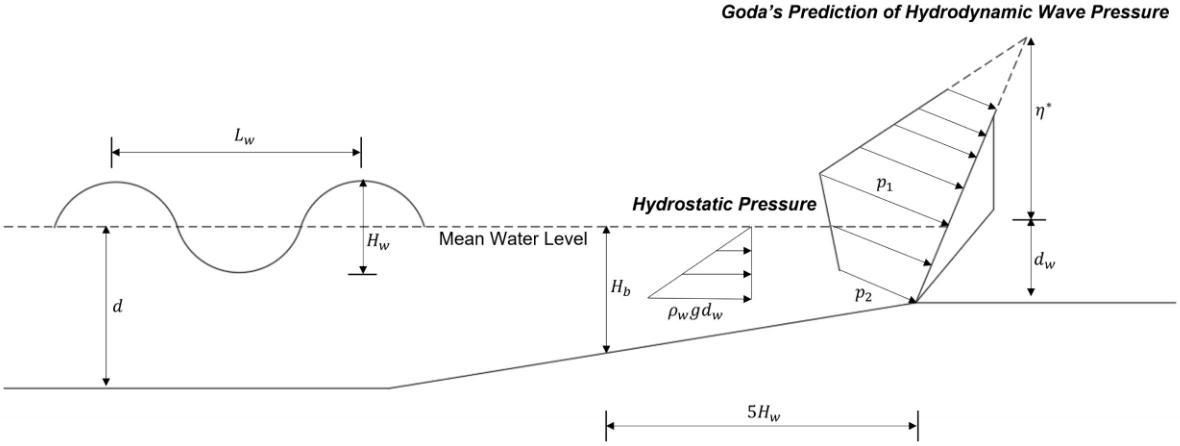

Fig. 2 Hydrostatic pressure and Goda's wave pressure

The wave pressure formula proposed by Goda [14–16] (Goda's formula) is one of the most popular empirical formulas to determine the wave pressure for wall-shaped coastal structures and it is the recommended design formula in Japan [25] and in Coastal Engineering Manual by United States Army Corps of Engineers (USACE) [26]. This empirical formula gives the maximum hydrodynamic wave loading for caissons, seawalls, and breakwaters with upright front face in the form of an equivalent static loading. Goda's formula takes different wave characteristics into account, such as water depth d, inundation height d_w, wave height H_w, wavelength L_w (wave period T_w can be calculated by the dispersion relationship of water waves) and bathymetry near the structure (Fig. 2). The linear dispersion relationship of water waves connecting T_w to L_w and d is as follows:

$$\left(\frac{2\pi}{T_w}\right)^2 = \frac{2\pi g}{L_w}\tanh\left(\frac{2\pi d}{L_w}\right) \tag{1}$$

where g denotes the gravitational acceleration. The distribution of wave pressure proposed by Goda follows a bilinear shape (Fig. 2), where the maximum pressure p_1 is reached at the mean water level. The mathematical form of Goda's formula is as follows:

$$\alpha_1 = 0.6 + \frac{1}{2}\left[\frac{4\pi d}{\sinh\left(\frac{4\pi d}{L_w}\right)L_w}\right]^2 \tag{2}$$

$$\alpha_2 = \min\left[\frac{h_b - d_w}{3h_b}\left(\frac{H_w}{d_w}\right)^2, \frac{2d_w}{H_w}\right] \tag{3}$$

$$\alpha_3 = 1 - \frac{d_w}{d}\left[1 - \frac{1}{\cosh\left(\frac{2\pi d}{L_w}\right)}\right] \tag{4}$$

$$p_1 = (\lambda_1\alpha_1 + \lambda_2\alpha_2)\rho_w g H_w \tag{5}$$

$$p_1 = \alpha_3 p_2 \tag{6}$$

$$\eta^* = 1.5H_w \tag{7}$$

where ρ_w denotes the water density, η^* is the wave runup on the structure, λ_1 and λ_2 are structural modification factors which are taken as 1 by default. For some of the scenarios where the steep front of the breaking wave exerts impulsive loading onto the structure, the α_2 coefficient should be replaced by the impulsive amplification coefficient α_I proposed by Takahashi et al. [25] if $\alpha_I > \alpha_2$. Herein, the influence of impulsive wave pressure will be discussed but the original form of Goda's formula instead of Takahashi's modification is used as the original form can account for a certain degree of wave breaking phenomenon. Beyond structures with upright flat surfaces, the formula has been proved with acceptable accuracy for structures with inclined flat surfaces by Tanimoto et al. [27]. Even though the applicability of Goda's formula has been extended over the past few decades, the extension has not been made to structures with complex geometry. Hence, Goda's formula will be evaluated herein to see if it is also applicable to hypar geometries.

2.2 Classification of Hydrodynamic Wave Loading

According to Kortenhaus and Oumeraci [28], the hydrodynamic wave loads can be categorized into different types based on their time histories (Fig. 3). The categorization is based on the ratio of the larger peak wave pressure $P_{w,max}$ to the smaller peak wave pressure $P_{w,qs}$ (Fig. 3) during each wave strike. When the wave is non-breaking, the hydrodynamic wave pressure is quasi-static and $\frac{P_{w,max}}{P_{w,qs}} \approx 1$ (Fig. 3.a). If the wave breaks in front of the structure, the impulsive feature of the wave pressure can be observed (Fig. 3.b) and $\frac{P_{w,max}}{P_{w,qs}} > 1$. The difference in wave characteristics, bathymetry and structural geometry greatly influence the types of wave loads applied on the structure, which will be further illustrated in Section 4.

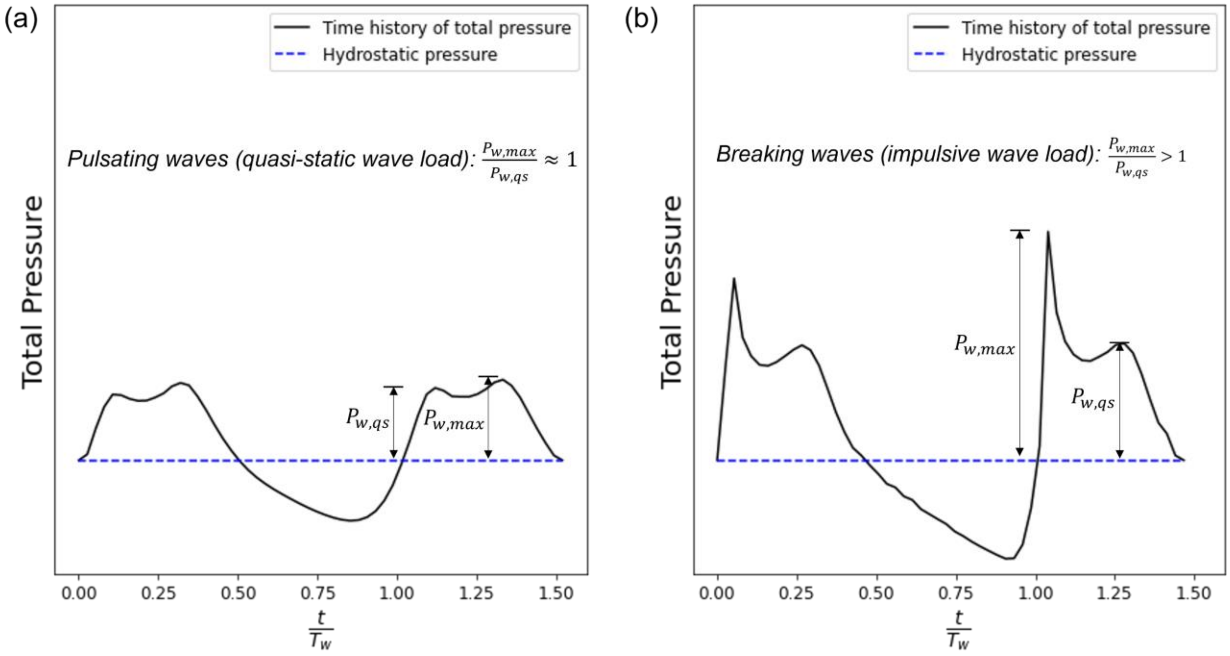

Fig. 3. Typical time history of wave loadings (t is the time, T_w is the wave period): a) Quasi-static wave loading induced by non-breaking waves; b) Impulsive wave loading induced by breaking waves

3 Decoupled SPH and FEM Modeling

According to Antoci et al. [29], for most coastal engineering applications, the structural deformation or displacement does not significantly influence the force exerted on the structure by the fluid flow and it is reasonable to view the structures as stationary objects in the numerical modeling of WSI. Moreover, a previous hydrostatic study [10] and the Hurricane Sandy case study [12] of thin-shell Kinetic Umbrella show that the maximum displacement of such structural system is on a millimeter or centimeter order of magnitude, which implies the small deformation of hypar shell as a coastal armor. Thus, a decoupled SPH-FEM scheme that treats the structures as stationary objects in the SPH modeling stage is proposed and implemented herein.

3.1 SPH Formulation

SPH was firstly introduced by Gingold and Monaghan [30] to solve problems in astrophysics and then extended to simulate free surface flows by Monaghan [31]. The basic idea of this method is to represent the continuum by a set of discrete particles and derive the physical quantities from conservation laws via kernel approximation.

3.1.1 SPH Approximation

In the continuum domain, any physical quantity $F(\boldsymbol{r})$ (velocity, density, pressure, etc.) at a specific location $\boldsymbol{r}$, is approximated by the integral of the product of a kernel function W with a corresponding smoothing length h and the physical quantity $F(\boldsymbol{r}')$ at position $\boldsymbol{r}'$ in the field:

$$F(\boldsymbol{r}) = \int F(\boldsymbol{r}')W(\boldsymbol{r}-\boldsymbol{r}',h)d\boldsymbol{r}' \tag{8}$$

Further approximation is then conducted after transforming the continuous form of Eq. (8) into the discrete form constructed by discrete particles:

$$F(\boldsymbol{r}) \approx \sum_j F(\boldsymbol{r}_j)W(\boldsymbol{r}-\boldsymbol{r}_j,h)\frac{m_j}{\rho_j} \tag{9}$$

where $\boldsymbol{r}_j$ denotes the position of any particle j that is close enough to this specific position $\boldsymbol{r}$, giving a non-zero kernel value $W(\boldsymbol{r}-\boldsymbol{r}_j,h)$; m_j, ρ_j are the mass and the density of particle j, respectively. The position vector $\boldsymbol{r}$ can be replaced by $\boldsymbol{r}_i$ to represent the particle i.

The kernel function $W(\boldsymbol{r}_{ij},h)$ determines the contribution of adjacent particle j to the calculation of $F(\boldsymbol{r}_i)$ based on the relative distance $q = \frac{\|r_{ij}\|_2}{h}$, where the $||\ ||_2$ sign is the Euclidean Norm of a vector and $\boldsymbol{r}_{ij} = \boldsymbol{r}_i - \boldsymbol{r}_j$. In this work, quintic kernel (a.k.a. Wendland kernel) [32] is used:

$$W(\boldsymbol{r}_{ij},h) = W_{ij} = \alpha_D\left(1-\frac{q}{2}\right)^4(2q+1) \qquad 0 \le q \le 2 \tag{10}$$

where α_D is $7h^2/4\pi$ in 2D domain and $21h^3/16\pi$ in 3D domain. The kernel value is zero elsewhere. The value of h is connected to the value of the initial distance of particles (dp) by $h = c_h\sqrt{3(dp)^2}$ (c_h is set as 1.2 herein for better wave propagation results [33]) and a smaller dp indicates a finer resolution of SPH.

3.1.2 Governing Equations and Time Stepping Algorithms

The motion of viscous fluid is described by Navier-Stokes momentum equations. Monaghan [34] proposed an artificial viscous term Π_{ij} in the discrete form of the momentum equation:

$$\frac{d\boldsymbol{v}_i}{dt} = \sum_j m_j \left(\frac{P_j}{\rho_j^2} + \frac{P_i}{\rho_i^2} + \Pi_{ij}\right) \nabla_i W_{ij} + \boldsymbol{g} \tag{11}$$

where $\boldsymbol{v}_i$ is the velocity, $P_{i,j}$ denotes the pressure, and ∇ is the gradient operator. Eq. (11) can be interpreted as the Newton's second law of a fluid particle, where the left-hand side is the acceleration of the particle i and the right-hand side calculates the force per unit mass. Π_{ij} is given by:

$$\Pi_{ij} = \begin{cases} \dfrac{-\alpha \bar{c}_{ij} \mu_{ij}}{\bar{\rho}_{ij}} & \boldsymbol{v}_{ij} \cdot \boldsymbol{r}_{ij} < 0 \\ 0 & \boldsymbol{v}_{ij} \cdot \boldsymbol{r}_{ij} > 0 \end{cases} \tag{12}$$

where $\boldsymbol{v}_{ij}$ represents the velocity difference between particle i and j, the μ_{ij} term is given by $\mu_{ij} = h \cdot \boldsymbol{v}_{ij} \cdot \boldsymbol{r}_{ij}/\left({r_{ij}}^2 + 0.1h\right)$, c_i denotes the speed of sound, $\bar{c}_{ij}$ and $\bar{\rho}_{ij}$ are the average speed of sound and average density, respectively. α is an empirical coefficient introducing the magnitude of dissipation and a value of 0.01 is proved to avoid instability and oscillations of the numerical results [21] and is subsequently used in this work.

For weakly-compressible SPH as used herein, the mass m_i is a constant and the density ρ_i changes according to the movement of particles given by the continuity equation, namely the conservation of mass:

$$\frac{d\rho_i}{dt} = \sum_j m_j \boldsymbol{v}_{ij} \cdot \nabla_i W_{ij} \tag{13}$$

To avoid density fluctuations so as to have accurate pressure values near the structure, the density diffusion term proposed by Fourtakas et al. [35] is applied to Eq. (13). The pressure value is connected to the density value and the relationship is given by the equation of state [36,37] as follows:

$$P = \frac{c_0^2 \rho_0}{7}\left[\left(\frac{\rho}{\rho_0}\right)^7 - 1\right] \tag{14}$$

where ρ_0 denotes the reference density and is taken as 1000 kg$\cdot\ m^{-3}$, and c_0 is the speed of sound at the reference density.

To numerically solve the governing Navier-Stokes equations, the symplectic position Verlet scheme [38] with a predictor-corrector stage is used. During each iteration, variable time step proposed by Monaghan and Kos [39] is used to satisfy the Courant-Friedrichs-Lewy (CFL) stability condition.

3.1.3 Boundary Particles and SPH-FEM Mapping

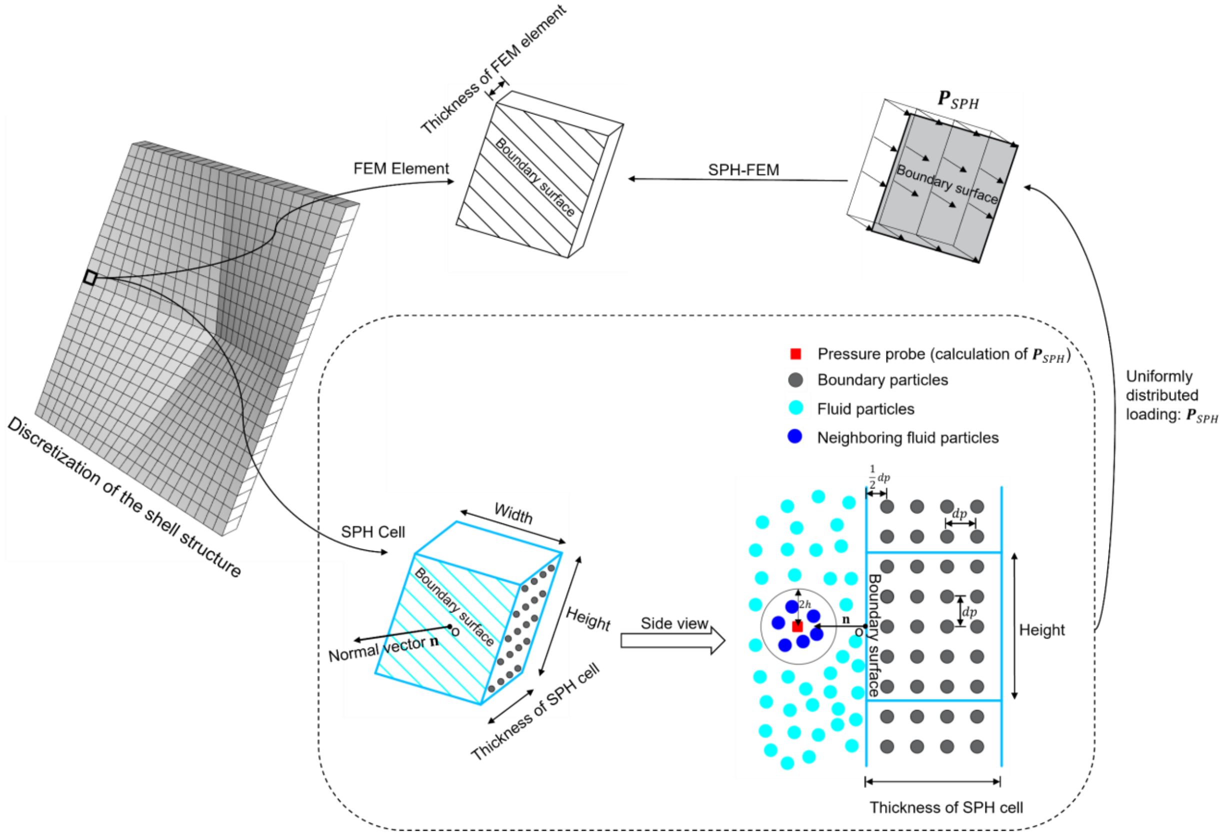

Fig. 4. Schematic of the SPH-FEM mapping

Besides fluid particles, the particles represent the structures in SPH modeling, referred as boundary particles, are of great significance. A generalized SPH-FEM mapping method for wave-shell interaction is proposed herein (Fig. 4). This mapping technique ensures the structural geometry is modeled correctly by the boundary particles in the SPH domain and transfers the wave pressure obtained from SPH to FEM for further structural analysis.

First, the shell structure is discretized into triangular or quadrilateral elements while the latter is implemented herein. The discretized shell element's surface that is in contact with the fluid is referred as the boundary surface. In the SPH domain, the boundary surface is extruded by a certain thickness to form a SPH cell, which contains a group of stationary boundary particles (Fig. 4) that are generated based on the choice of resolution dp [19]. These boundary particles satisfy the same governing equations as fluid particles [17], but they stay still and do not move like the fluid particles. When the fluid particles approach the boundary particles, the density of the boundary particles increases, and the pressure increases accordingly, providing repulsive force to fluid particles. Note that the thickness of the SPH cell is not related to the actual structural element, whereas the thickness is recommended to include enough layers of boundary particles (layers $\geq \frac{2h}{dp}$) to achieve better accuracy of SPH modeling [40].

The next step is to map the corresponding loads calculated from SPH modeling to FE models (Fig. 4). One pressure probe is placed normal to the center of the boundary surface to calculate the pressure $\boldsymbol{P}_{SPH}$ based on the pressure values of neighboring fluid particles:

$$\boldsymbol{P}_{SPH} = \boldsymbol{P}_i = \frac{\sum_j \boldsymbol{P}_j W(\boldsymbol{r}_{ij}, h)}{\sum_j W(\boldsymbol{r}_{ij}, h)} \tag{15}$$

where $\boldsymbol{P}_i$ represents the pressure at the pressure probe and j here is the subscript for all the neighboring fluid particles. The distance between the pressure probe and the boundary surface is on the order of h, which can be obtained by a sensitivity study. By assuming the wave loading on each shell element is evenly distributed, uniform pressure $\boldsymbol{P}_{SPH}$ is applied on each FEM shell element. The boundary particles are configured with Modified Dynamic Boundary Conditions (mDBC) [41] instead of Dynamic Boundary Conditions (DBC) [17] because the use of mDBC significantly decreases the unrealistic gap between fluid and boundary particles encountered by DBC setup, enabling accurate position determination of pressure probes in front of the SPH cells.

The technique implemented herein is different from the decoupled SPH-FEM method by Wang et al. [8], in which the force $\boldsymbol{f}_{SPH}$ obtained from one SPH cell is applied as a nodal force to the shared joint of four FEM elements and $\boldsymbol{f}_{SPH}$ is calculated by:

$$\boldsymbol{f}_{SPH} = \sum_b m_b \frac{d\boldsymbol{v}_b}{dt} \tag{16}$$

where m_b is the mass, $\frac{d\boldsymbol{v}_b}{dt}$ is the acceleration of the boundary particle b within a SPH cell and $\boldsymbol{f}_{SPH}$ is the total force of a cell. It is appropriate to use Eq. (16) to calculate the total reaction force of a full structure because an enough number of boundary particles will be included for a full structure as was done by Wang et al. [8]. However, since the present study focuses on the detailed pressure distribution, the newly proposed method (Eq. (15) and Fig. 4) is more appropriate. The reason is twofold: first of all, in the previous technique, one SPH cell is mapped to four FEM elements so that they do not have one-to-one correspondence; second, Eq. (16) does not use the kernel approximation and requires extremely small dp to include enough boundary particles inside one SPH cell for an accurate result. In contrast, the newly proposed method does not require extremely small dp because the nature of kernel approximation enables calculating the pressure using more neighboring fluid particles near the pressure probe and it has one-to-one correspondence of the SPH cell and the FEM element. As a result, the newly proposed method is more robust and more computationally efficient. This mapping technique can be extended to any shell-type structures with complex geometry.

3.1.4 Wave Generation

The open boundary condition proposed for weakly compressible SPH method in [42] is used to generate waves instead of using DBC modeled piston. The advantages of using open boundary include saving computational time because the fluid domain can be reduced from of 3-4 wavelengths to only one wavelength long [43,44] and mitigating the effect of reflected waves from DBC modeled piston [44]. The velocity imposed on fluid particles in the open boundary to generate waves is calculated according to the wavemaker theory by Madsen [45].

3.2 Structural Dynamic Analysis via FEM

In the previous study of Kinetic Umbrellas [12], the maximum loading obtained from SPH modeling is applied statically on the structure, which ignores the dynamic feature of WSI. In this way, the critical demands of the structures may be underestimated. It is more appropriate to conduct structural dynamic analysis using the time history of the total pressure.

Direct integration is chosen and Newmark method [46] that corresponds to Average Acceleration Method is used for time stepping. Proportional damping is implemented for the consideration of damping effects:

$$\mathbf{C}=\alpha\mathbf{M}+\beta\mathbf{K} \tag{17}$$

where **C**, **M** and **K** are the damping matrix, mass matrix and stiffness matrix in the equation of motion, respectively; α and β are mass-proportional and stiffness-proportional damping coefficient, respectively. The values of α and β are calculated so that a damping ratio (ξ) of 0.05 is reached at ω_1 and $\omega_{90\%}$, where ω_1 is the natural frequency of the first mode of the structure and $\omega_{90\%}$ is the natural frequency of the mode at which 90% of modal participating mass ratio has been accumulated. In this way, the damping ratios for modes with a frequency between ω_1 and $\omega_{90\%}$ will be smaller than 5% because the damping ratio ξ_n for the nth mode with the frequency ω_n is given as:

$$\xi_n = \frac{1}{2\omega_n}\alpha + \frac{\omega_n}{2}\beta \tag{18}$$

4 Parametric Study

A parametric study implementing the decoupled SPH-FEM technique is illustrated in this section, where the parameters are related to wave characteristics and structural geometries.

4.1 Parametric Study Setup

4.1.1 Structures and FEM Configurations

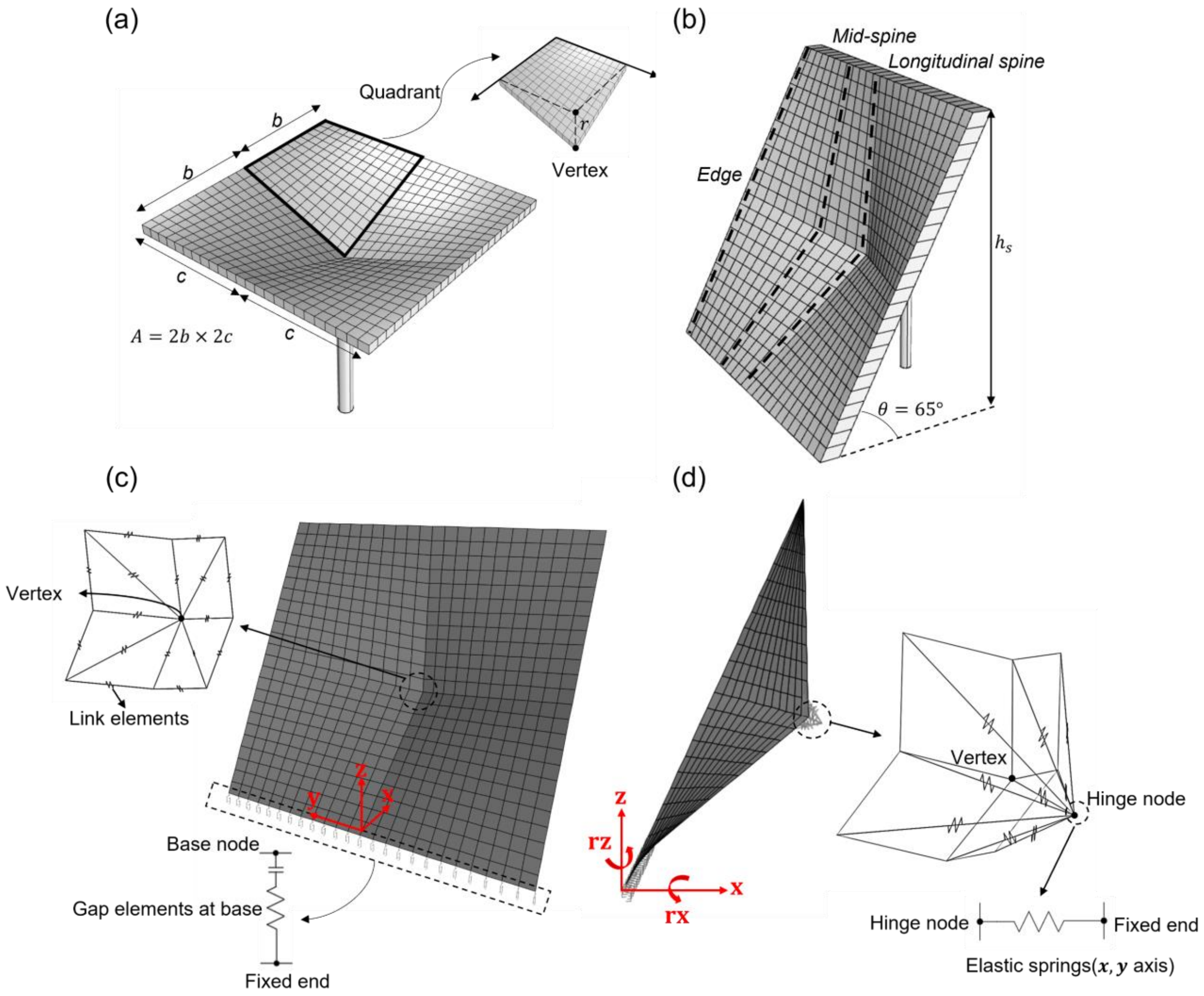

Fig. 5. a) Geometric parameters of the umbrella; b) Geometric parameters of the shell seawall; c) & d) Overview of the FE model

Parameters	Values	Units
$b = c$	3.2, 4	m
h_s	5.8, 7.25	m
r/A	0, 0.03, 0.045	1/m

Table 1 Parameters of Structural Geometries

Inclined flat-surface and hypar-shaped Kinetic Umbrellas are considered in the parametric study. Generalized geometric description for flat-surface and hypar geometries can be seen in Fig. 5.a, and interested readers are referred to the work by Wang et al. [8] for details. The parameters b and c represent the edge lengths, which are set as identical in this study; r is the rise of the vertex relative to the plane formed by the edges and a value of zero yields a flat surface; the ratio r/A quantifies the warping magnitude of hypar, where A is the area of the plane formed by the four edges. The angle of inclination θ is taken as 65° in this study. h_s is the structural height, which can be calculated by the values of b and θ. The parameters selected herein are summarized in Table 1. To look for generalized findings, two sets of structural heights are chosen by changing the value of b and keeping θ as a constant to enlarge the data sets and three sets of warping ratios are considered to see how warping magnitude influences the wave pressure and structural response.

In terms of FEM configurations, the shell is discretized into 576 quadrilateral Mindlin/Reissner-type shell elements with a thickness of 100 mm (Fig. 5.c), where the number of FEM elements is selected according to a sensitivity study in [8]. The material of the shell and the support column is high-strength concrete with a compressive strength f_c' of 65Mpa and a Young's modulus E_c of 37900Mpa. At the base nodes (Fig. 5.c) of the structure, gap elements are implemented, simulating the structure resting on a base that permits the displacement in the positive **z** direction. The distance between the vertex node and the hinge node is taken as 0.3m and link elements with an arbitrarily large Young's modulus are used to connect the shell nodes near the hinge zone and the hinge node with the shell nodes (Fig. 5.d). The hinge node is restrained along the **z**, **rx**, and **rz** directions to model the rotation of the hinge and the vertical resistance of the support column. Elastic springs with a stiffness calculated by $k_s = \frac{3E_c I_s}{h_{sc}^3}$ are assigned to the hinge node along **x** and **y** directions to model the transverse stiffness of the 1.2m square support column (Fig. 5.d), where I_s is the moment of inertia and h_{sc} is the height of the support column.

The settings of structural dynamic analysis have been discussed in Section 3.2. One dynamic analysis case is with proportional damping and the other is undamped. Three static analyses are also conducted: the maximum pressure at each pressure probe in SPH modeling is applied statically in one case, the second one applies the theoretical hydrostatic pressure together with Goda's prediction of the hydrodynamic wave pressure and the third case only applies the theoretical hydrostatic pressure. The finite element analysis is conducted using SAP2000 v20 [47].

4.1.2 Bathymetry, Waves and SPH Configurations

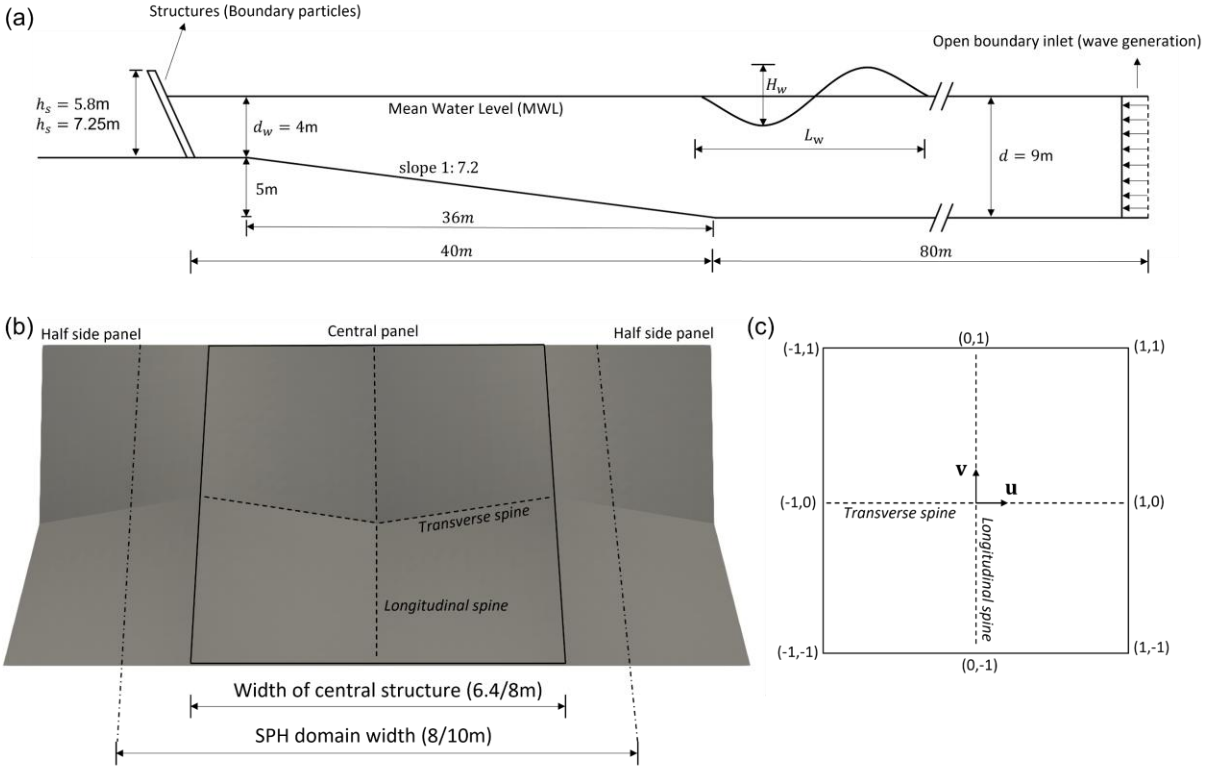

Fig. 6. a) Side view of the SPH domain; b) Front view of the SPH boundary cells; c) Planar projected view and normalized local coordinate system

The bathymetry implemented herein (Fig. 6.a) is a modification of a beach profile (#17901) at Monmouth Beach as recorded in New Jersey Beach Profile Network (NJBPN). The water depth d is 9m and the inundation d_w is set as 4m in front of the structure, which can be interpreted via two realistic scenarios: a breakwater located on a berm (neglecting the inundation on the back), or a seawall on the beach that encounters high intensity of storm surge. Non-breaking and breaking regular waves are considered in this study (Table 2). The wave height H_w ranges from 1 to 3m and the wave period T_w ranges from 6 to 9s (Table 2). The approximate wavelength L_w (Table 2) is calculated by the linear dispersion relationship (Eq. (1). The length of the SPH domain with a constant water depth (80m) is set to be greater than the maximum wavelength, permitting satisfying wave generation [44]. Furthermore, the wave characteristics selected comply with the condition $U < \frac{8\pi^2}{3}$ as specified in Madsen's wavemaker theory [45], where $U = \frac{H_w {L_w}^2}{d^3}$ is the Ursell number indicating the nonlinearity of the waves.

$\boldsymbol{H_w}$(m) / $\boldsymbol{T_w}$(s)	1	2	3	$\boldsymbol{L_w}$(m)
6	Non-breaking waves	Non-breaking waves	Breaking waves	46.9
7.5				62.8
9				78.2

Table 2 Parameters of Regular Wave Characteristics

Since Kinetic Umbrellas work as a continuous structural system along the shoreline, parts of adjacent structures are modeled alongside the central structure in the SPH domain (Fig. 6.b). The width of the domain (Fig. 6.b) is selected based on a sensitivity study of the pressure along the edge of the central structure to ensure the boundary condition is modeled correctly. The domain widths of 8m and 10m correspond to the seawall height $h_s = 5.8$m and 7.25m, respectively. The structure is placed on a berm with a front slope of 1:7.2. The initial distance of particle (dp) is set to be 0.12m based on a preliminary sensitivity study of the pressure value on the structure and the thickness of the boundary SPH cell is set to be 1.5m. Based on the choice of dp, there are around 6/7 million particles initially generated in the domain. The physical simulation time is set to be 50 seconds, allowing sufficient wave strikes on the structure. 576 pressure probes are placed in front of 576 SPH cells with a distance of $1.5h$ to capture the time history of the pressure exerted on the structure. The representative of the total pressure P_{total} at each pressure probe is taken as the peak pressure over time: $P_{total} = \max_{0 \le t \le 50} P(t)$, and the representative hydrodynamic wave pressure P_{wave} is obtained by subtracting the theoretical hydrostatic pressure P_{static} from the total pressure: $P_{wave} = P_{total} - P_{static}$. All the SPH simulations in DualSPHysics are conducted utilizing NVIDIA GPUs with parallel computing CUDA cores via Princeton University's Della Cluster, which significantly reduces the computational time needed. The simulation time is around 10-12 hours using a NVIDIA A100 GPU and around 20 hours on a personal laptop with a GeForce RTX 3080 GPU for each case.

4.2 Validation of SPH Scheme

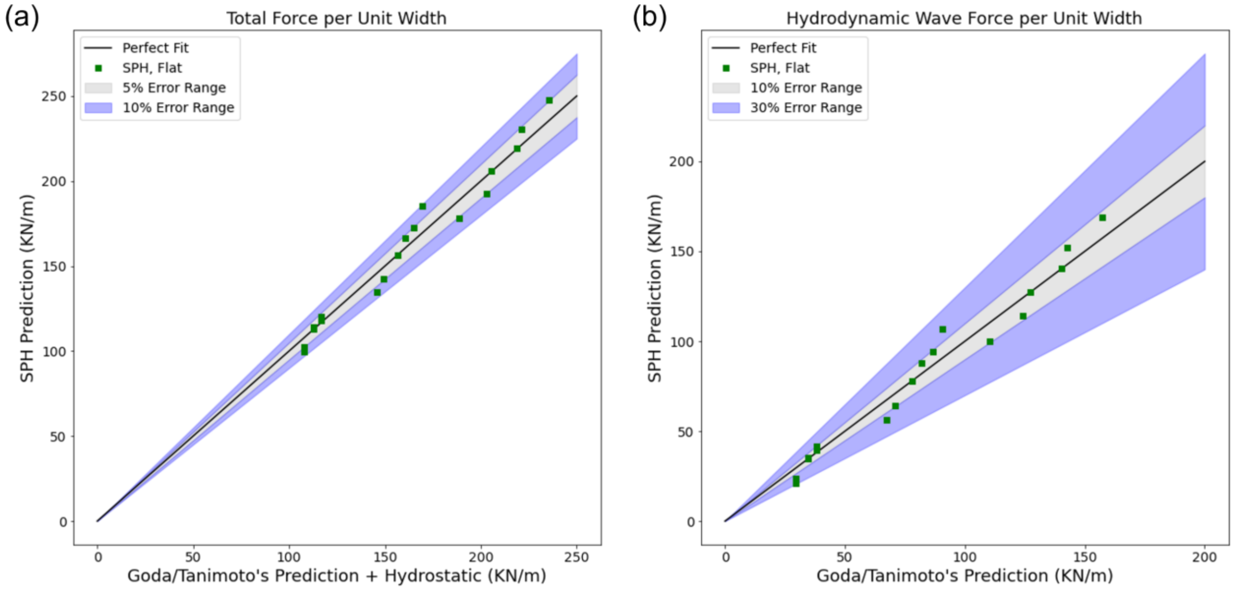

Fig. 7 Validation of the SPH scheme via the comparison between SPH's and Goda/Tanimoto's prediction for flat-surface geometry: a) Total force per unit width; b) Hydrodynamic wave force per unit width

Validation is conducted before analyzing the results obtained from SPH modeling. Since Goda's formula has been proved by Tanimoto et al. [48] to be capable of estimating the wave pressure on structures with inclined flat surface, the validation is made by comparing the SPH results and Goda's prediction for the wave force exerted on inclined flat surface.

Fig. 7 presents the comparison between SPH and Goda's prediction in terms of the force per unit width, which is obtained by the integration of pressure values (P_{total} or P_{wave}) over height. The data points represent the variation of parameters from Table 1 and Table 2 with r/A = 0.00m^{-1} (flat surface). It can be seen from Fig. 7.a that for the total force per unit width, the difference between SPH's and Goda's prediction is mostly smaller than 5%. For hydrodynamic wave force prediction, the difference is mainly smaller than 10%. As a result, the SPH configuration is valid and the results from SPH modeling can be further analyzed and discussed.

4.3 Results of Hydrodynamic Wave Pressure

4.3.1 Spatial Distribution of the Wave Pressure and the Influence of Geometries

For hypar geometries, the hydrodynamic wave pressures along the edge, mid-spine and longitudinal spine (Fig. 5.b) are first selected to partially reflect the spatial distribution and to be compared with flat surface seawalls. Fig. 8 illustrates the hydrodynamic wave pressure P_{wave} on smaller-size structures (h_s = 5.8m) with different wave heights and constant T_w = 7.5s. The hydrodynamic wave pressure on hypar geometries generally follows a bilinear shape where the maximum pressure over the height is reached near the mean water level (MWL), similar to the pattern predicted by Goda's formula. The hydrodynamic wave pressure along hypar's longitudinal spine is larger than that of the mid-spine, and the edge of hypar has the minimum pressure. This phenomenon is not that significant when the waves are non-breaking and exert quasi-static wave pressure (Fig. 3.a). When the wave height is relatively large ($H_w = 3$m) and induces impulsive breaking wave load (Fig. 3.b), the positive pressure deviation from the edge to the longitudinal spine of hypar is intensified (Fig. 8.c). Comparing hypar and flat surface, it can be also observed that the pressure along the edge of hypar is close to that of flat-surface structure for nearly all wave characteristics. With the increase of hypar's warping magnitude (r/A) from 0.03m^{-1} to 0.045m^{-1}, the pressure does not increase or slightly increases for non-breaking waves (Fig. 8.a and b) and increases significantly for breaking waves (Fig. 8.c) near the longitudinal spine.

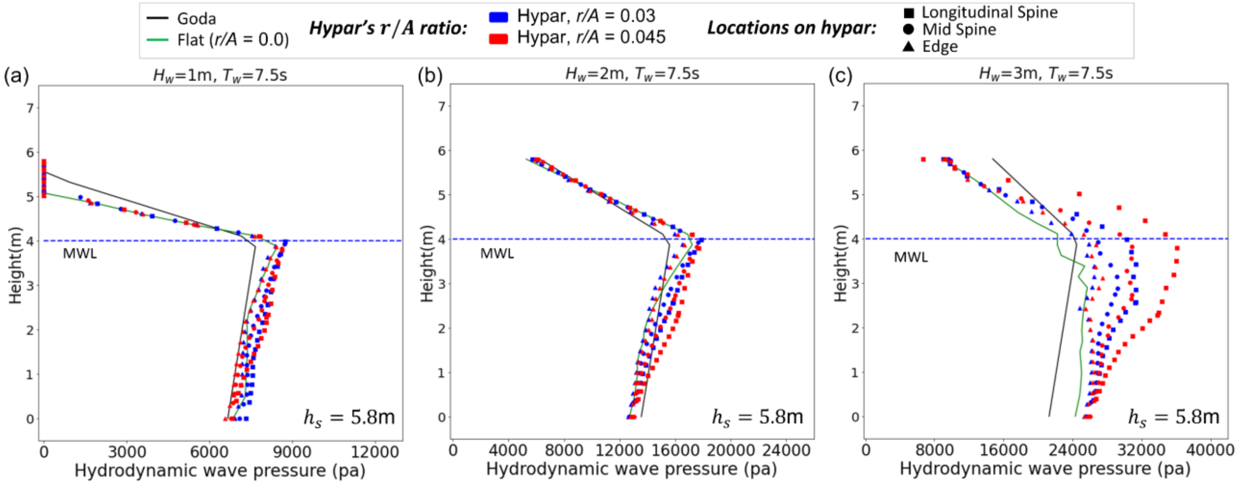

Fig. 8 Hydrodynamic wave pressure on structures with the structural height (h_s) of 5.8m: a) $H_w = 1$m, $T_w = 7.5$s (non-breaking); b) $H_w = 2$m, $T_w = 7.5$s (non-breaking); c) $H_w = 3$m, $T_w = 7.5$s (breaking)

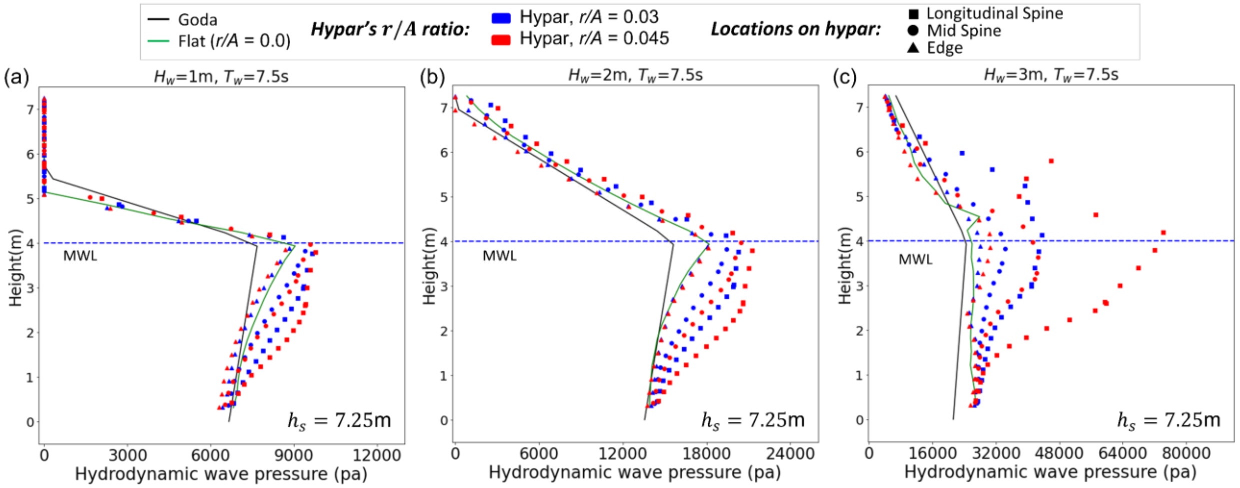

Fig. 9 Hydrodynamic wave pressure on structures with the structural height (h_s) of 7.25m: a) $H_w = 1$m, $T_w = 7.5$s (non-breaking); b) $H_w = 2$m, $T_w = 7.5$s (non-breaking); c) $H_w = 3$m, $T_w = 7.5$s (breaking)

For taller structures with h_s of 7.25m, similar bilinear hydrodynamic wave pressure distribution can be observed (Fig. 9) for hypar structures. When the wave breaks, likewise, a much larger wave pressure (Fig. 9.c) is exerted near the longitudinal spine of the hypar with higher warping magnitude (r/A = 0.045m^{-1}) when compared to hypar with smaller warping magnitude.

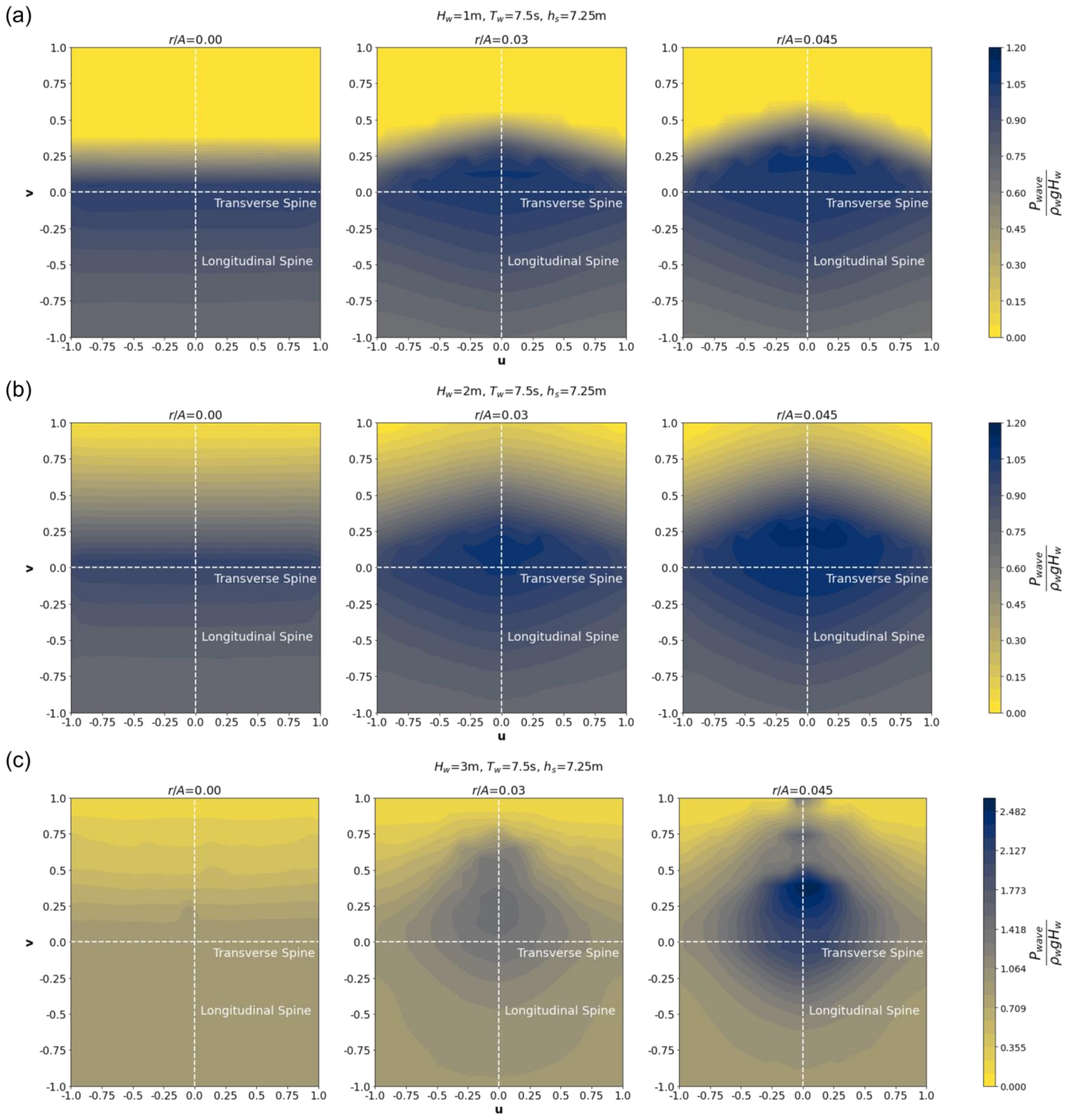

Fig. 10 Spatial distribution of the normalized hydrodynamic wave pressure $\frac{P_{wave}}{\rho_w g H_w}$ exerted on different structures (h_s=7.25m, T_w=7.5s): a) $H_w = 1$m; b) $H_w = 2$m; c) $H_w = 3$m

To explain the findings above and to have a more comprehensive view of the spatial distribution of the hydrodynamic wave pressure exerted on different structures, the contour plot of the nondimensional wave pressure $\frac{P_{wave}}{\rho_w g H_w}$ is drawn (Fig. 10) for h_s = 7.25m and T_w = 7.5s (similar trends can be found for other cases). The local coordinate system (Fig. 6.c) is used where u is the normalized horizontal distance to the longitudinal spine and v is the normalized vertical distance to the transverse spine in the planar projected plane. In addition, Fig. 11 and Fig. 12 are the interpretations of Fig. 10 by presenting three snapshots in SPH modeling at times when (a) the wave approaches the structure, (b) induces the highest peak wave pressure and (c) runs up on the structure.

For flat surface (r/A = 0.00m^{-1}), as expected, $\frac{P_{wave}}{\rho_w g H_w}$ does not change along the **u** axis (Fig. 10). When hypar geometry is introduced, the contour lines form a series of diamond shape, which shows that the hydrodynamic wave pressure increases gradually from the edge to the longitudinal spine (Fig. 10). This phenomenon is due to the warping feature of hypar and can be explained from a physical point of view: the warping of the hypar leads to the acceleration of incoming waves towards the longitudinal spine so that a high velocity is achieved near this region, resulting in an increase of hydrodynamic wave pressure locally. Fig. 11 and Fig. 12 clearly show that the warping feature of hypar makes the peak velocity higher near the spine than near the edge. The magnitude of this spatial difference of hydrodynamic wave pressure on hypar is sensitive to wave types. When non-breaking waves strike, the maximum normalized hydrodynamic wave

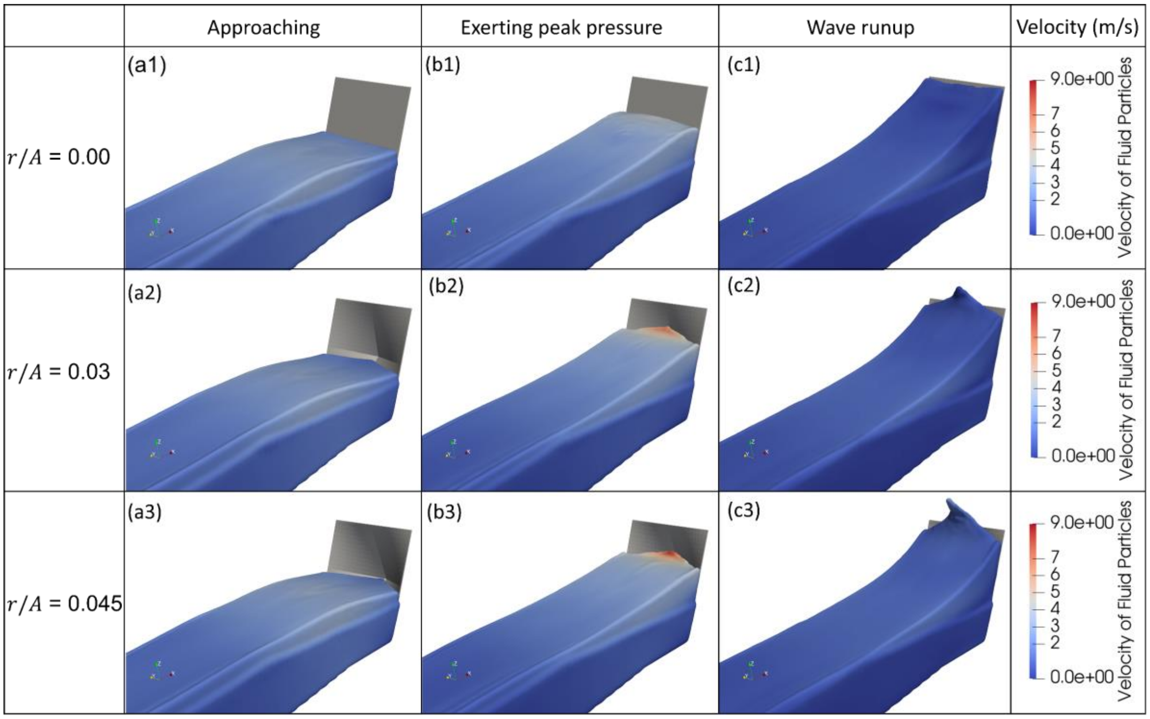

Fig. 11 Snapshots of SPH Modeling for $H_w = 2$m, $T = 7.5$s (non-breaking wave), $h_s = 7.25$m

pressure ($\frac{P_{wave}}{\rho_w g H_w}$) along hypar's spine is approximately 1.0 to 1.2 (Fig. 10.b & Fig. 10.c) while it is around 0.9 to 1.0 along the edge, and the small deviation in the velocity of fluid particles can explain the small difference in the hydrodynamic wave pressure (Fig. 11.b2, Fig. 11.b3). However, when the wave breaks, the peak velocity near the longitudinal spine can be as much as 27 m/s while the peak velocity near the edge is around 5 to 10 m/s (Fig. 12.b3), resulting in a more significant pressure difference at the longitudinal spine and the edge: for r/A = 0.03m^{-1}, $\frac{P_{wave}}{\rho_w g H_w}$ along the spine is around 1.4 to 1.6 while it is approximately 0.8 to 1.0 along the edge (Fig. 12.b2); for r/A = 0.045m^{-1}, $\frac{P_{wave}}{\rho_w g H_w}$ is around 2.4 to 2.6 near the longitudinal spine while it is approximately 1.0 to 1.2 along the edge (Fig. 12.b3).

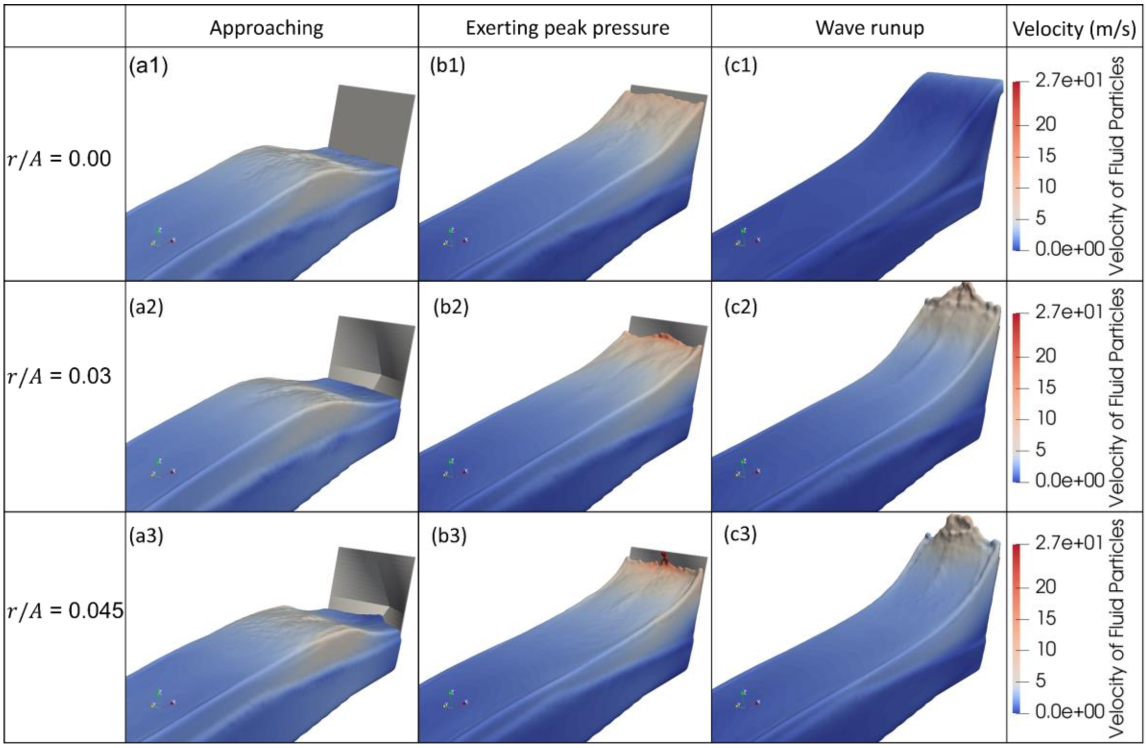

Fig. 12 Snapshots of SPH Modeling for $H_w = 3$m, $T = 7.5$s (breaking wave), $h_s = 7.25$m

The influence of r/A on hydrodynamic wave pressure is also sensitive to wave types. As can be seen in Fig. 10.a and Fig. 10.b, the maximum hydrodynamic wave pressure on hypar with r/A = 0.03m^{-1} and r/A = 0.045m^{-1} is around the same, because the peak velocity does not vary much for these cases with non-breaking waves (Fig. 11). When the wave starts to break before hitting the structure ($H_w = 3$m, $T = 7.5$s), the maximum velocity reaches a value of around 27 m/s (Fig. 12.b3) for hypar with $r/A = 0.045$m^{-1} while the maximum value is approximately 16 m/s (Fig. 12.b2) when $r/A = 0.03$m^{-1}, explaining a much higher $\frac{P_{wave}}{\rho_w g H_w}$ (2.4 to 2.6) on hypar with higher warping magnitude ($r/A = 0.045$m^{-1}) when compared to the structure with a smaller warping ratio ($r/A = 0.03$m^{-1}) where the maximum hydrodynamic wave pressure is around 1.4 to 1.6 $\rho_w g H_w$. The overturning crest of a breaking wave accelerates while approaching the structure, which is exacerbated by the increased r/A ratio, yielding larger impact velocities and leading to a large impulsive wave pressure near the longitudinal spine.

4.3.2 Applicability of Goda's Formula to Hypar Geometry

In terms of the applicability of Goda's formula to hypar geometry, it can be seen in Fig. 8 and Fig. 9 that the bilinear shape of hydrodynamic wave pressure distribution along height is predicted by the formula. For non-breaking waves with quasi-static wave pressure ($H_w = 1, 2$m), the values of wave pressure predicted by Goda's formula are close to numerical results. However, there exists a clear pattern of slightly underestimating the wave pressure values for locations along mid-spine and longitudinal spine by Goda's formula when compared to SPH results. This implies that shape modification factors (λ_1 and λ_2) greater than 1 should be used in Goda's formula (Eq. (5) to predict the hydrodynamic wave pressure on locations away from the edges of hypar. When the wave breaks ($H_w = 3$m) and impulsive loading occurs, Goda's formula without Takahashi's impulsive force coefficient α_I [49] still predicts the hydrodynamic wave pressure for flat-surface close to numerical results, but it underestimates the hydrodynamic wave pressure for hypar significantly, especially near the spine and for hypar with high r/A ratio (Fig. 8.c, Fig. 9.c). This shows that a combination of higher shape modification factors (λ_1, λ_2) and impulsive force coefficients (a_I) is needed to predict the breaking wave pressure near hypar's spine when hypar has a large value of rise (r) due to its size (h_s) and warping magnitude (r/A).

Fig. 13 summarizes the results of the force per unit width on hypar geometry from SPH modeling and Goda's prediction. With the increase of the wave height, the hydrodynamic wave force increases accordingly. With the increase of the wave period, the hydrodynamic wave force of non-breaking waves increases as the increased wave period indicates higher wavelength and higher energy. However, when the wave breaks, the influence of the wave period is more complicated because when and where the wave starts to break and how it interacts with the structure significantly influence the impulsive breaking wave load. The wave with smaller period may even exert higher impulsive force on the structure as one can see in Fig. 13.d. The difference between Goda's prediction and SPH is mostly below 10% for both the total force (Fig. 13.a) and the wave force (Fig. 13.c) when the structural height (h_s) is 5.8m. As the structural height increases to 7.25m, the difference is also mostly smaller than 10% for total force (Fig. 13.b) but more points lie outside of the 10% bar (Fig. 13.d) for wave force prediction. It shows that Goda's formula is a good candidate for estimating the hydrodynamic wave pressure on hypar-shaped seawall when extremely large impulsive force (Fig. 3.b) is not present as the outliers mostly come from the cases when H_w = 3m.

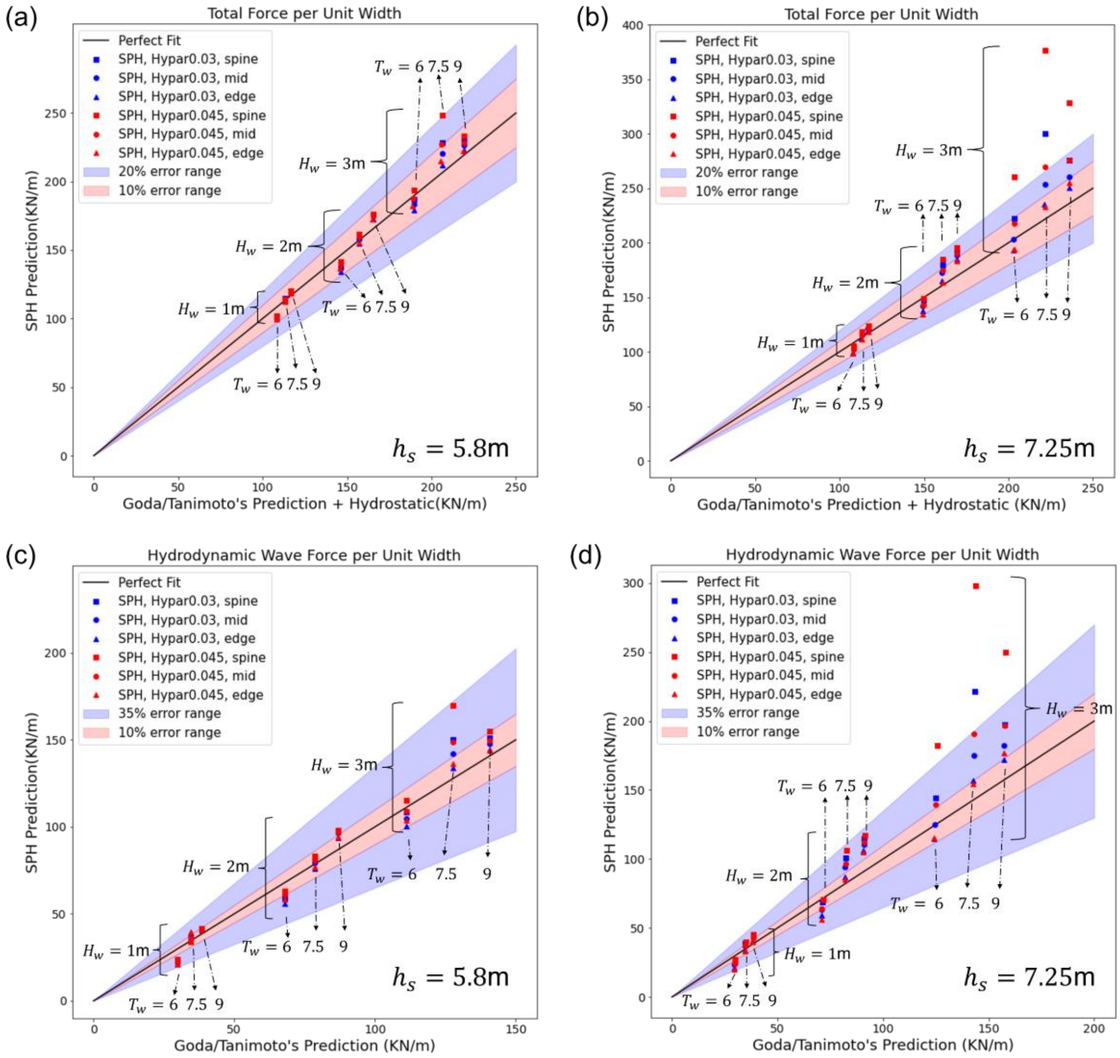

Fig. 13 Summary of the force prediction from SPH and Goda's formula for hypar geometries: a) Total force per unit width, $h_s = 5.8$m; b) Total force per unit width, $h_s = 7.25$m; c) Hydrodynamic wave force per unit width, $h_s = 5.8$m; d) Hydrodynamic wave force per unit width, $h_s = 7.25$m

4.4 Results of Structural Response

The decoupled SPH-FEM technique introduced in Section 3.1.3 enables the analysis of structural response under different wave conditions for different structures. Critical shell demands such as maximum shell moment (M^*_{shell}), maximum transverse shear force (V^*_{shell}), maximum membrane forces (N^C_{shell}, N^T_{shell}) and maximum shell displacement (δ^*_{max}), as well as critical demands for the support column such as shear force (V^*_{col}), base moment (M^*_{col}) and axial force (N^*_{col}) are discussed in the following paragraphs. Note that if tensile axial force in the support column is present, it is viewed as the critical demand herein since uplift in the foundation is not ideal.

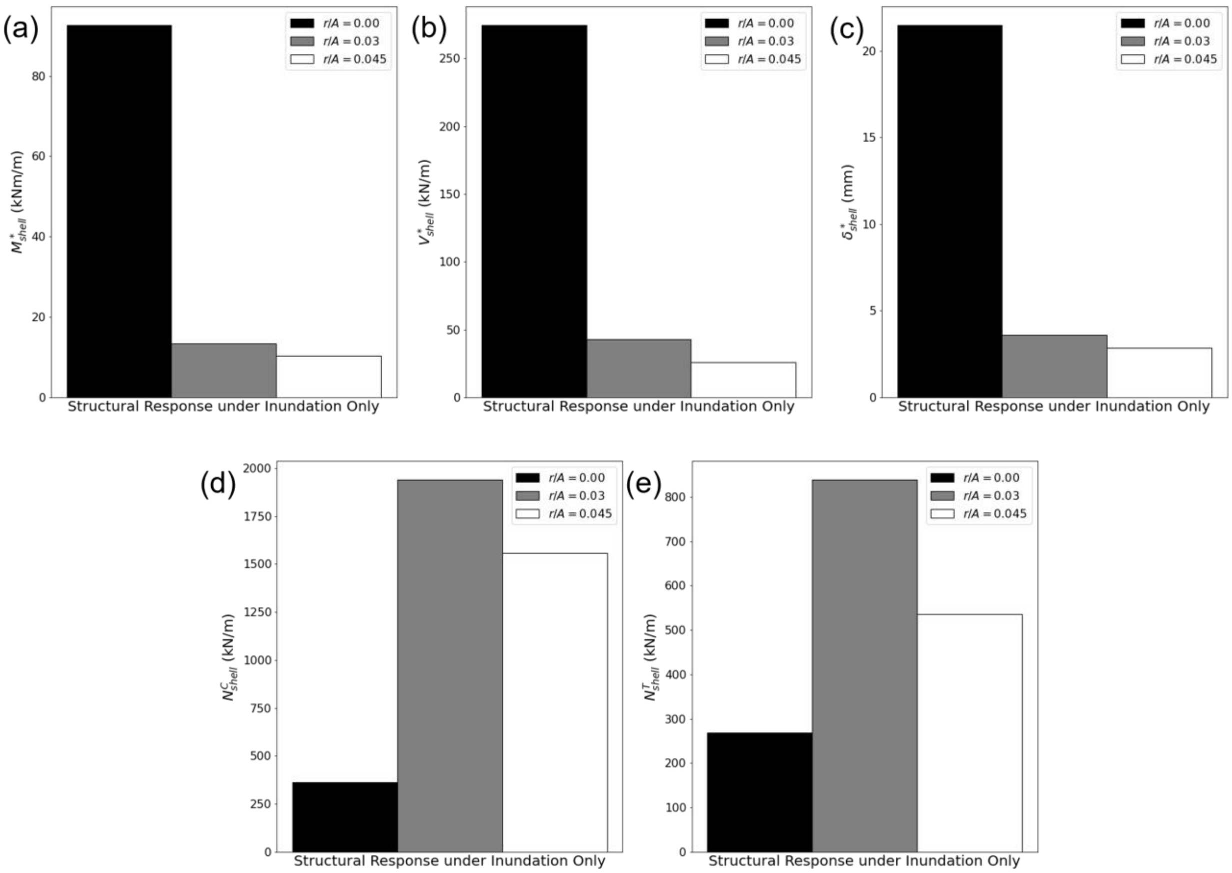

Fig. 14 Critical demands of structures (h_s = 7.25m) under hydrostatic inundation: a) maximum shell bending moment (M^*_{shell}); b) maximum transverse shear force (V^*_{shell}); c) maximum shell displacement (δ^*_{shell}); d) maximum membrane compressive axial force (N^C_{shell}); e) maximum membrane tensile axial force (N^T_{shell})

To first see how differently hypar geometries and flat surface behave, the critical shell demands under hydrostatic inundation are summarized in Fig. 14 for structures with $h_s = 7.25$m. Similar to the results reported in [10] and as expected, without hypar geometries (r/A = 0.00m^{-1}), extremely high values of M^*_{shell} (Fig. 14.a) and V^*_{shell} (Fig. 14.b) are present on the shell structure, which emphasizes that thin shell with flat surface is not qualified as coastal armor, because flat geometries behave like a flat slab where the out-of-plane internal forces are high while in-plane internal forces are rather low. With the introduction of hypar geometries (r/A = 0.03m^{-1}, 0.045m^{-1}) where the double-curvature is present, the high demands in M^*_{shell} and V^*_{shell} decrease significantly while an increase in membrane internal forces ($N^C_{shell},\ N^T_{shell}$) can be observed, implying the mechanism in resisting the loads has changed from beam to truss action after introducing the hypar geometry. Clearly, hypar is much more structurally efficient and enables a better use of the concrete shell since the compressive in-plane membrane behavior is ideal while the out-of-plane behavior is unwanted. Moreover, the maximum displacement present on the shell decreases from more than 2cm to less than 5mm by using hypar geometries. In the following discussion, flat-surface geometries will not be further discussed since these geometries do not behave ideally even only against hydrostatic loading.

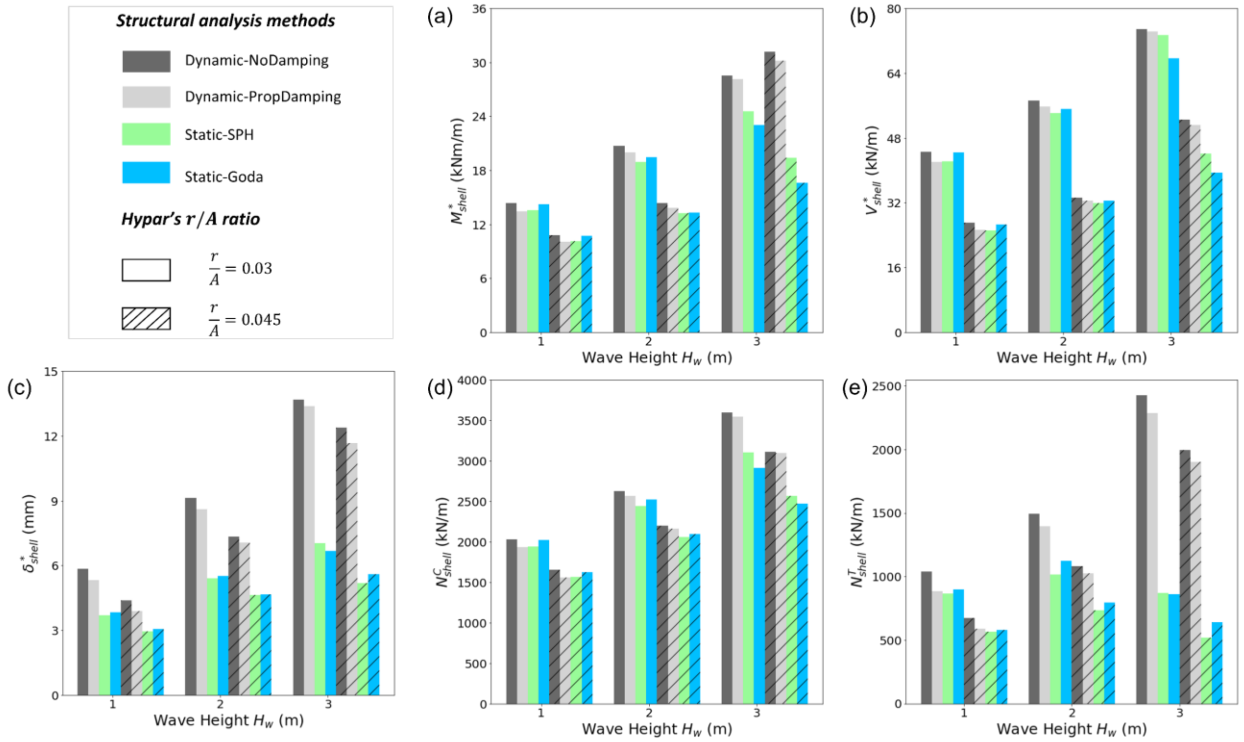

Fig. 15 Critical demands of hypar shells (h_s = 7.25m, T_w =7.5s): a) Maximum bending moment M^*_{shell}; b) Maximum out-of-plane shear force V^*_{shell}; c) Maximum displacement δ^*_{shell}; d) Maximum in-plane compressive axial force N^C_{shell}; e) Maximum in-plane tensile axial force N^T_{shell}

Fig. 15 summarizes the critical demands of shells while $h_s = 7.25$m and $T_w = 7.5$s for different wave heights, warping magnitudes, and analysis methods. First, it can be concluded that the critical demands from dynamic structural analyses are mostly larger than or close to their static counterparts that use the maximum pressure from SPH modeling (Static-SPH). For non-breaking waves, the critical demands obtained from dynamic analyses are only slightly larger than or close to the static analyses for M^*_{shell}, V^*_{shell} and N^C_{shell}, which shows that these critical demands are not sensitive to analysis methods when the wave pressure is nearly quasi-static. However, as the wave breaks and generates impulsive breaking wave load (Fig. 3.b) on the structure, critical demands like M^*_{shell} and N^C_{shell} are sensitive to the methods of analysis. For instance, when $H_w = 3$m and r/A = 0.03m^{-1} (Fig. 15.a), the difference is of around 15% between dynamic analysis (with damping) and its static counterpart in predicting the maximum shell bending moment (M^*_{shell}). When $H_w = 3$m and r/A = 0.045m^{-1} (Fig. 15.a), M^*_{shell} is 30.15 kNm/m using dynamic analysis (with damping) while the static analysis (Static-SPH) only gives a value of 19.42 kNm/m, which is a difference of 55.3%. The difference in N^T_{shell} is large when the wave height is greater than 1m, showing that the static analysis significantly underestimates the tensile axial deformation of the shell. Regardless of the wave characteristics, the difference in δ^*_{max} is large between static and dynamic analyses (Fig. 15.c), which is expected since the influence of inertial force is taken into consideration in dynamic analysis, enlarging the displacement when the spring force is along the opposite direction as the inertial force. It is important to note that the maximum displacement is on the order of centimeter or millimeter, showing that the setting of stationary structures in SPH modeling is valid even with the consideration of dynamics.

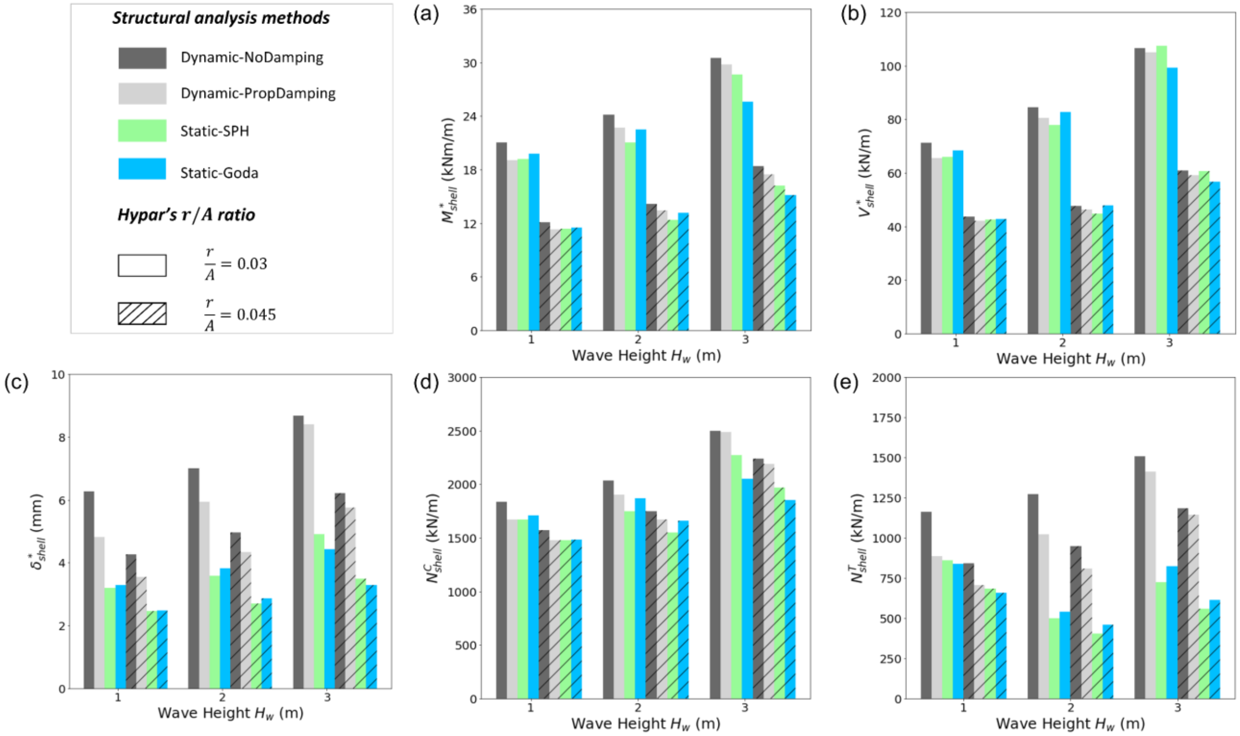

Fig. 16 Critical demands of hypar shells (h_s = 6.4m, T_w =7.5s): a) Maximum bending moment M^*_{shell}; b) Maximum out-of-plane shear force V^*_{shell}; c) Maximum displacement δ^*_{shell}; d) Maximum in-plane compressive axial force N^C_{shell}; e) Maximum in-plane tensile axial force N^T_{shell}

For h_s = 6.4m (Fig. 16), similar findings can be observed but the difference in M^*_{shell} between static and dynamic analyses is not that significant when the wave breaks, which is because the breaking wave force is not that significant compared to when $h_s = 7.25$m as one can see in Fig. 8.c and Fig. 9.c. Comparing the analyses with and without damping, it can be seen from Fig. 15 and Fig. 16 that the dynamic analyses without damping predict slightly higher critical demands compared to cases with damping. It is because the transient response (free vibration) component of the structure will not be damped out in models without damping, but the transient response is relatively small compared to the steady-state response (forced vibration) so that damping does not make a significant difference.

Fig. 17 summarizes the critical demands of the support column when $T_w = 7.5$s, and it can be observed that for V^*_{col} and M^*_{col}, there is not a significant difference between static and dynamic analyses. However, in terms of N^*_{col}, the static analysis is not capable of capturing the possible uplift force that may govern the design the foundation underneath, which implies the necessity of a time history analysis.

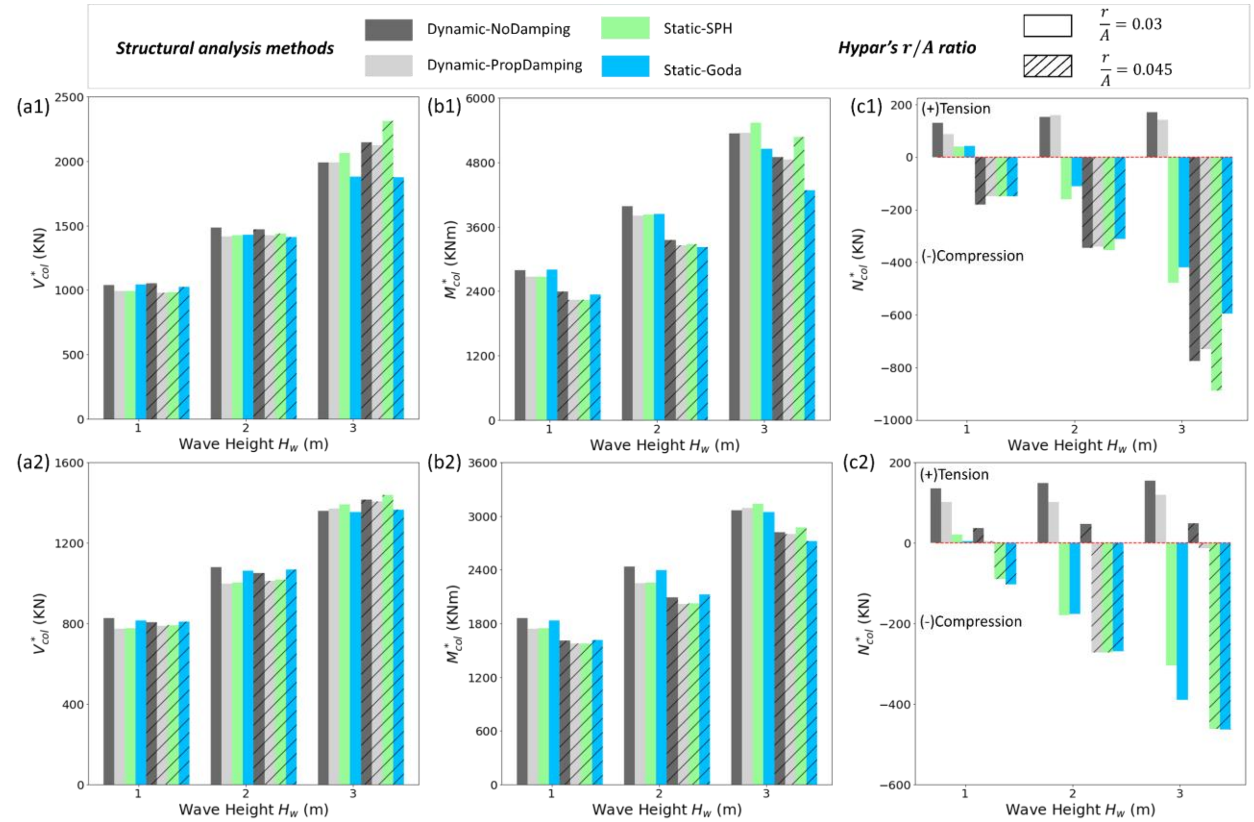

Fig. 17 Critical demands of support columns of hypar shells (T_w =7.5s): a1), b1) & c1) Shear force V^*_{col}, base moment M^*_{col}, and axial force N^*_{col} (positive: tension, negative: compression) when h_s = 7.25m; a2), b2) & c2) Shear force V^*_{col}, base moment M^*_{col}, and axial force N^*_{col} (positive: tension, negative: compression) when h_s = 6.4m

To evaluate if Goda's formula can be implemented to design and analyze such kinds of thin shell structures for coastal defense, the critical demands obtained by applying SPH pressure and Goda's formula along with hydrostatic pressure are compared and summarized for all the cases in Fig. 18. The difference is mostly smaller than 10% for predicting M^*_{shell}, V^*_{shell}, N^C_{shell}, V^*_{col} and M^*_{col}, showing that the static analysis with this empirical formula captures these structural responses quite accurately. δ^*_{shell} and N^T_{shell} are greatly underestimated by such static analysis and the possible uplift force in the support column is sometimes ignored. Nevertheless, static analysis with Goda's formula can be viewed as a valid tool for preliminarily designing such kinds of coastal structures, but the designers should be cautious about the critical demands that will be underestimated or neglected by statically applying Goda's pressure prediction.

Comparing hypar geometries with different r/A ratios (Fig. 14, Fig. 15, Fig. 16), it is observed that hypar with higher warping magnitudes are more structurally efficient, since the critical demands for hypar with r/A = 0.045m^{-1} are smaller than hypar with r/A = 0.03m^{-1} for most of the cases where the wave loadings are relatively close for these geometries. This shows that the increased concavity of the structure enables a smaller deformation of the shell if the loadings are around the same, reducing the internal forces. However, since hypar with higher r/A ratio may be subjected to larger impulsive force from breaking waves, some critical demands of these structures may be larger than the structures with smaller r/A ratio despite of their capability of mitigating the shell deformation. For instance, when H_w = 3m, T_w = 7.5s and h_s = 7.25m, the wave pressure for hypar with r/A = 0.045m^{-1} is much larger than hypar with r/A = 0.03m^{-1} (Fig. 9.c), and subsequently M^*_{shell} is larger for hypar with r/A = 0.045m^{-1} (Fig. 15).

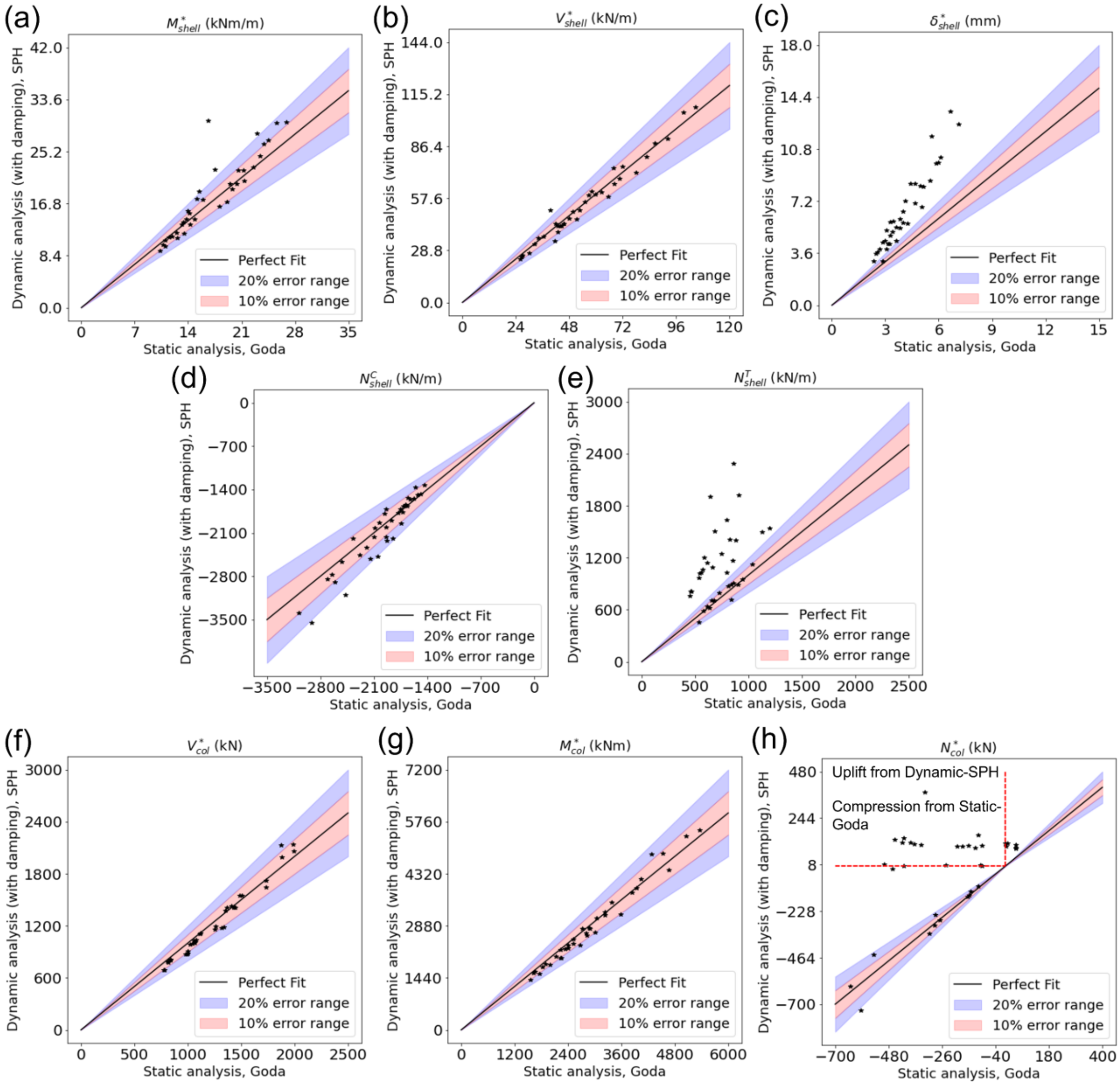

Fig. 18 Comparison between dynamic analysis (loads: maximum total pressure obtained from SPH) and static analysis (loads: Goda's pressure plus hydrostatic pressure) in predicting critical structural demands

The reinforcement design of the concrete shell and the support column is not the focus of this study and the readers are referred to the work by Wang et al. [8,10] for details. To briefly illustrate the structural feasibility, the flexural moment capacity of the 100mm thick concrete shell with 16 mm diameter glass fiber reinforced polymer (GFRP) bars is 41 kNm/m using the configuration in [8], which is larger than 31.2 kNm/m, the maximum M^*_{shell} presented in this study. If greater demands of the shell are needed due to more severe hydrodynamic wave loading and hydrostatic loading, the thickness of the shell can be increased accordingly. For instance, by increasing the shell thickness to 150mm, the flexural moment capacity of the shell can be improved to 112kNm/m [12].

5 Conclusions

To facilitate the employment of hypar thin shells for coastal defense as a sustainable alternative to traditional coastal structures, a decoupled SPH-FEM analysis is conducted herein. A modified SPH-FEM mapping technique based on Wang et al. [8] is introduced first, which enables generating satisfying results without the need of extremely small value of dp. Later, SPH models are configurated and validated by comparing the numerical results to Goda's formula. After validating the SPH scheme, models with different wave characteristics and structural geometries are built to parametrically study the wave pressure distribution on structures. Implementing the SPH-FEM mapping technique, FEM analyses are conducted and the critical demands of the shell as well as the support column are summarized. Based on the results, the difference between static and dynamic analyses and the structural efficiency of hypar shells with different r/A ratios are illustrated. In addition, the applicability of Goda's formula to the analysis of hypar shells against waves is also evaluated. The conclusions are as follows:

- The hydrodynamic wave pressure on hypar follows a bilinear-like shape along the height of the structure where the maximum wave pressure is reached near the mean water level. The hydrodynamic wave pressure decreases transversely from the longitudinal spine to the edge of hypar and the hydrodynamic wave pressure along the edge of hypar is close to that of a flat surface.
- The positive pressure deviation from the edge to the longitudinal spine is not significant when the wave is non-breaking and when the r/A ratio is small. When the wave breaks and generates impulsive wave load, such pressure deviation will be intensified, resulting in very large pressure near the longitudinal spine. With the increase of r/A, such pressure deviation will also be magnified.
- Static structural analyses underestimate the critical demands of N^T_{shell} and δ^*_{shell} significantly when compared to dynamic analyses, and they may not capture the potential uplift force in the support column that may happen when the wave strikes. Moreover, when the impulsive wave loads are dominant, static analyses will greatly underestimate M^*_{shell} and N^C_{shell}.

- Goda's formula is a good candidate for predicting the hydrodynamic wave pressure on hypar structures, but higher shape modification factors (λ_1, λ_2) should be applied when predicting the pressure near the longitudinal spine of hypar. When the wave breaks, a combination of impulsive force coefficient (a_I) and higher shape modification factors (λ_1, λ_2) are needed. Furthermore, static structural analysis with Goda's formula can be used for preliminary design and analysis purposes, but further dynamic analysis is needed to capture all the critical demands.

By addressing the knowledge gaps in previous studies [8,10,12], this paper gains newer insight into hypar thin shell resisting wave loading. However, it must be pointed out that the implemented SPH simulation is single-phase so that future research on breaking wave force on hypar with the consideration of air entrapment is needed. Geotechnical design of the foundation, structural optimization of Kinetic Umbrellas and experimental tests are also required. Nevertheless, this paper establishes a solid foundation for the employment of hypar thin shells as countermeasures against extreme events like storm surges. With the kinetic feature, this lightweight structural system is a way to provide reliable protection while trying to minimize the negative environmental, economic, and social impacts brought by coastal structures. Also, the decoupled SPH-FEM technique implemented herein is a handy tool to study wave-shell interaction and can be potentially extended for a wider range of wave-structure interaction (WSI) problems that are of great significance in the context of climate change.

CRediT authorship contribution statement

Gaoyuan Wu: Conceptualization, Methodology, Software, Validation, Formal analysis, Writing – original draft, review & editing. **Maria Garlock**: Conceptualization, Writing – review & editing, Supervision, Funding acquisition. **Shengzhe Wang**: Conceptualization, Writing – review & editing

Declaration of Competing Interest

The authors declare that they have no known competing financial interests or personal relationships that could have appeared to influence the work reported in this paper.

Acknowledgements

Funding for this research was partially sponsored by Princeton University through the "Project X" grant and the Metropolis Project of Princeton University.

References

[1] Connor T, Niall R, Cummings P, Papillo M. Incorporating Climate Change Adaptation into Engineering Design Concepts and Solutions. Australian Journal of Structural Engineering 2013;14:125–34. https://doi.org/10.7158/13287982.2013.11465127.

[2] Bitner-Gregersen EM, Eide LI, Hørte T, Skjong R. Ship and Offshore Structure Design in Climate Change Perspective. Berlin, Heidelberg: Springer Berlin Heidelberg; 2013. https://doi.org/10.1007/978-3-642-34138-0.

[3] Nicholls RJ, Cazenave A. Sea-Level Rise and Its Impact on Coastal Zones. Science 2010.

[4] Olsen JR. Adapting Infrastructure and Civil Engineering Practice to a Changing Climate. Reston, VA: American Society of Civil Engineers; 2015. https://doi.org/10.1061/9780784479193.

[5] Dugan JE, Airoldi L, Chapman MG, Walker SJ, Schlacher T, Wolanski E, et al. 8.02-Estuarine and coastal structures: environmental effects, a focus on shore and nearshore structures. Treatise on Estuarine and Coastal Science 2011;8:17–41.

[6] Bastidas-Arteaga E, Schoefs F. Sustainable maintenance and repair of RC coastal structures. Proceedings of the Institution of Civil Engineers-Maritime Engineering, vol. 168, Thomas Telford Ltd; 2015, p. 162–73.

[7] Kimura S. When a seawall is visible: Infrastructure and obstruction in post-tsunami reconstruction in Japan. Science as Culture 2016;25:23–43.

[8] Wang S, Garlock M, Glisic B. Hydrostatic Response of Deployable Hyperbolic-Paraboloid Umbrellas as Coastal Armor. J Struct Eng 2020;146:04020096. https://doi.org/10.1061/(ASCE)ST.1943-541X.0002619.

[9] Wang S, Garlock M, Glisic B. Parametric Modeling of Depth-Limited Wave Spectra under Hurricane Conditions with Applications to Kinetic Umbrellas against Storm Surge Inundation. Water 2021;13:251. https://doi.org/10.3390/w13030251.

[10] Wang S, Notario V, Garlock M, Glisic B. Parameterization of hydrostatic behavior of deployable hypar umbrellas as flood barriers. Thin-Walled Structures 2021;163:107650. https://doi.org/10.1016/j.tws.2021.107650.

[11] Wang S, Garlock M, Glisic B. Kinematics of deployable hyperbolic paraboloid umbrellas. Engineering Structures 2021;244:112750. https://doi.org/10.1016/j.engstruct.2021.112750.

[12] Wang S, Garlock M, Glisic B, Deike L. Feasibility of kinetic umbrellas as deployable flood barriers during landfalling hurricanes. J Struct Eng 2022;148. https://doi.org/10.1061/(ASCE)ST.1943-541X.0003295.

[13] Meyer C. The greening of the concrete industry. Cement and Concrete Composites 2009;31:601–5. https://doi.org/10.1016/j.cemconcomp.2008.12.010.

[14] Goda Y. NEW WAVE PRESSURE FORMULAE FOR COMPOSITE BREAKWATERS. COASTAL ENGINEERING n.d.:19.

[15] Goda Y. Experiments on the transition from nonbreaking to postbreaking wave pressures. Coastal Engineering in Japan 1972;15:81–90.

[16] Goda Y. Random Seas And Design Of Maritime Structures (3rd Edition). World Scientific Publishing Company; 2010.

[17] Crespo AJC, Domínguez JM, Rogers BD, Gómez-Gesteira M, Longshaw S, Canelas R, et al. DualSPHysics: Open-source parallel CFD solver based on Smoothed Particle Hydrodynamics (SPH). Computer Physics Communications 2015;187:204–16. https://doi.org/10.1016/j.cpc.2014.10.004.

[18] Liu MB, Liu GR. Smoothed Particle Hydrodynamics (SPH): an Overview and Recent Developments. Arch Computat Methods Eng 2010;17:25–76. https://doi.org/10.1007/s11831-010-9040-7.

[19] Domínguez JM, Crespo AJC, Barreiro A, Gómez-Gesteira M, Mayrhofer A. Development of a new pre-processing tool for SPH models with complex geometries. 6th International SPHERIC workshop, 2011, p. 117–24.

[20] Crespo AC, Dominguez JM, Barreiro A, Gómez-Gesteira M, Rogers BD. GPUs, a New Tool of Acceleration in CFD: Efficiency and Reliability on Smoothed Particle Hydrodynamics Methods. PLoS ONE 2011;6:e20685. https://doi.org/10.1371/journal.pone.0020685.

[21] Altomare C, Crespo AJC, Domínguez JM, Gómez-Gesteira M, Suzuki T, Verwaest T. Applicability of Smoothed Particle Hydrodynamics for estimation of sea wave impact on coastal structures. Coastal Engineering 2015;96:1–12. https://doi.org/10.1016/j.coastaleng.2014.11.001.

[22] Barreiro A, Crespo AJC, Domínguez JM, Gómez-Gesteira M. Smoothed Particle Hydrodynamics for coastal engineering problems. Computers & Structures 2013;120:96–106. https://doi.org/10.1016/j.compstruc.2013.02.010.

[23] Zhang F, Crespo A, Altomare C, Dominguez J, Marzeddu A, Shang S, et al. DualSPHysics: a numerical tool to simulate real breakwaters. Journal of Hydrodynamics 2018.

[24] Dang B-L, Nguyen-Xuan H, Abdel Wahab M. Numerical study on wave forces and overtopping over various seawall structures using advanced SPH-based method. Engineering Structures 2021;226:111349. https://doi.org/10.1016/j.engstruct.2020.111349.

[25] Japan Ports and Harbours Bureau, Ministry of Land, Infrastructure, Transport and Tourism, Port and Airport Research Institute. Technical standards and commentaries for port and harbour facilities in Japan. The Overseas Coastal Area Development Institute of Japan (OCDI); 2020.

[26] US Army Corps of Engineers. Coastal engineering manual. US Army Corps of Engineers Washington, DC; 2002.

[27] Tanimoto K, Kimura K. A Hydraulic Experimental Study on Trapezoidal Caisson Breakwaters. The Port and Harbour Research Institute, Ministry of Transport, Japan; 1985.

[28] Kortenhaus A, Oumeraci H. Classification of Wave Loading on Monolithic Coastal Structures. Coastal Engineering 1998, Copenhagen, Denmark: American Society of Civil Engineers; 1999, p. 867–80. https://doi.org/10.1061/9780784404119.064.

[29] Antoci C, Gallati M, Sibilla S. Numerical simulation of fluid–structure interaction by SPH. Computers & Structures 2007;85:879–90. https://doi.org/10.1016/j.compstruc.2007.01.002.

[30] Gingold RA, Monaghan JJ. Smoothed particle hydrodynamics: theory and application to non-spherical stars. Monthly Notices of the Royal Astronomical Society 1977;181:375–89. https://doi.org/10.1093/mnras/181.3.375.

[31] Monaghan JJ. Simulating Free Surface Flows with SPH. Journal of Computational Physics 1994;110:399–406. https://doi.org/10.1006/jcph.1994.1034.

[32] Wendland H. Piecewise polynomial, positive definite and compactly supported radial functions of minimal degree. Advances in Computational Mathematics 1995;4:389–96.

[33] Altomare C, Domínguez JM, Crespo AJC, González-Cao J, Suzuki T, Gómez-Gesteira M, et al. Long-crested wave generation and absorption for SPH-based DualSPHysics model. Coastal Engineering 2017;127:37–54. https://doi.org/10.1016/j.coastaleng.2017.06.004.

[34] Monaghan JJ. Smoothed Particle Hydrodynamics. Annual Review of Astronomy and Astrophysics 1992;30:543–74. https://doi.org/10.1146/annurev.aa.30.090192.002551.

[35] Fourtakas G, Vacondio R, Alonso JD, Rogers BD. Improved density diffusion term for long duration wave propagation. 2020 SPHERIC Harbin International Workshop, 2020.

[36] Batchelor CK, Batchelor GK. An introduction to fluid dynamics. Cambridge university press; 2000.

[37] Monaghan JJ, Cas RA, Kos AM, Hallworth M. Gravity currents descending a ramp in a stratified tank. Journal of Fluid Mechanics 1999;379:39–69.

[38] Leimkuhler B, Matthews C. Molecular Dynamics. Springer; 2016.

[39] Monaghan JJ, Kos A. Solitary Waves on a Cretan Beach. Journal of Waterway, Port, Coastal, and Ocean Engineering 1999;125:145–55. https://doi.org/10.1061/(ASCE)0733-950X(1999)125:3(145).

[40] Fourtakas G, Dominguez JM, Vacondio R, Rogers BD. Local uniform stencil (LUST) boundary condition for arbitrary 3-D boundaries in parallel smoothed particle hydrodynamics (SPH) models. Computers & Fluids 2019;190:346–61.

[41] English A, Domínguez JM, Vacondio R, Crespo AJC, Stansby PK, Lind SJ, et al. Modified dynamic boundary conditions (mDBC) for general-purpose smoothed particle hydrodynamics (SPH): application to tank sloshing, dam break and fish pass problems. Comp Part Mech 2021. https://doi.org/10.1007/s40571-021-00403-3.

[42] Tafuni A, Domínguez JM, Vacondio R, Crespo AJC. A versatile algorithm for the treatment of open boundary conditions in Smoothed particle hydrodynamics GPU models. Computer Methods in Applied Mechanics and Engineering 2018;342:604–24. https://doi.org/10.1016/j.cma.2018.08.004.

[43] Verbrugghe T, Dominguez JM, Altomare C, Tafuni A, Troch P, Kortenhaus A. Application of open boundaries within a two-way coupled SPH model to simulate non-linear wave-structure interactions. Coastal Engineering Proceedings 2018:14–14.

[44] Verbrugghe T, Domínguez JM, Altomare C, Tafuni A, Vacondio R, Troch P, et al. Non-linear wave generation and absorption using open boundaries within DualSPHysics. Computer Physics Communications 2019;240:46–59. https://doi.org/10.1016/j.cpc.2019.02.003.

[45] Madsen OS. On the generation of long waves. Journal of Geophysical Research (1896-1977) 1971;76:8672–83. https://doi.org/10.1029/JC076i036p08672.

[46] Newmark NM. A method of computation for structural dynamics. Journal of the Engineering Mechanics Division 1959;85:67–94.

[47] CSI S. CSI analysis reference manual. I: Berkeley (CA, USA): Computers and Structures INC 2014.

[48] a hydraulic experimental study on trapezoidal caisson breakwaters.pdf n.d.

[49] TAKAHASHI S. A proposal of impulsive pressure coefficient for design of composite breakwaters. Proc Int Conf Hydro- Tech Eng Port Harbor Constr (Hydro-Port ’94) 1994:489–504.